



NRC Publications Archive Archives des publications du CNRC

Free Volume in Molten and Glassy Polymers and Nanocomposites Utracki, Leszek A.

Publisher's version / Version de l'éditeur:

Polymer Physics: From Suspensions to Nanocomposites and Beyond, pp. 553-604, 2010-08-01

NRC Publications Record / Notice d'Archives des publications de CNRC:

<https://nrc-publications.canada.ca/eng/view/object/?id=585473ad-0974-43b4-b73e-210a913129c0>
<https://publications-cnrc.canada.ca/fra/voir/objet/?id=585473ad-0974-43b4-b73e-210a913129c0>

Access and use of this website and the material on it are subject to the Terms and Conditions set forth at

<https://nrc-publications.canada.ca/eng/copyright>

READ THESE TERMS AND CONDITIONS CAREFULLY BEFORE USING THIS WEBSITE.

L'accès à ce site Web et l'utilisation de son contenu sont assujettis aux conditions présentées dans le site

<https://publications-cnrc.canada.ca/fra/droits>

LISEZ CES CONDITIONS ATTENTIVEMENT AVANT D'UTILISER CE SITE WEB.

Questions? Contact the NRC Publications Archive team at

PublicationsArchive-ArchivesPublications@nrc-cnrc.gc.ca. If you wish to email the authors directly, please see the first page of the publication for their contact information.

Vous avez des questions? Nous pouvons vous aider. Pour communiquer directement avec un auteur, consultez la première page de la revue dans laquelle son article a été publié afin de trouver ses coordonnées. Si vous n'arrivez pas à les repérer, communiquez avec nous à PublicationsArchive-ArchivesPublications@nrc-cnrc.gc.ca.



14

FREE VOLUME IN MOLTEN AND GLASSY POLYMERS AND NANOCOMPOSITES

LESZEK A. UTRACKI

National Research Council Canada, Industrial Materials Institute, Boucherville, Quebec, Canada

- 14.1 Introduction
 - 14.1.1 Free volume in polymeric nanocomposites
 - 14.1.2 Pressure–volume–temperature measurements
- 14.2 Theory
 - 14.2.1 Molten state
 - 14.2.2 Glass and other transitions
 - 14.2.3 The vitreous state
- 14.3 PVT behavior and derivatives
 - 14.3.1 PVT of amorphous polymers and their CPNCs
 - 14.3.2 PVT of semicrystalline polymers and their CPNCs
 - 14.3.3 Compressibility coefficient, κ
 - 14.3.4 Thermal expansion coefficient, α
 - 14.3.5 Compressibility and thermal expansion of PA-6 and its CPNCs
- 14.4 Free-volume content and interaction parameters
 - 14.4.1 Single-phase liquids
 - 14.4.2 Polymeric nanocomposites
 - 14.4.3 Free volume in PNCs
 - 14.4.4 Lennard–Jones binary interaction parameters
 - 14.4.5 Structure and transitions within the molten phase
- 14.5 Free volume in the glassy state
 - 14.5.1 Glass transition temperature region
 - 14.5.2 Glassy state of amorphous polymers
- 14.6 Summary and conclusions

Polymer Physics: From Suspensions to Nanocomposites and Beyond, Edited by Leszek A. Utracki and Alexander M. Jamieson
Copyright © 2010 John Wiley & Sons, Inc.

14.1 INTRODUCTION

14.1.1 Free Volume in Polymeric Nanocomposites

The free-volume concept dates back to the Clausius [1880] equation of state. The need for postulating the presence of occupied and free space in a material has been imposed by the fluid behavior. Only recently has positron annihilation lifetime spectroscopy (PALS; see Chapters 10 to 12) provided direct evidence of free-volume presence. Chapter 6 traces the evolution of equations of state up to derivation of the configurational hole–cell theory [Simha and Somcynsky, 1969; Somcynsky and Simha, 1971], in which the lattice hole fraction, h , a measure of the free-volume content, is given explicitly. Extracted from the pressure–volume–temperature (PVT) data, the dependence, $h = h(T, P)$, has been used successfully for the interpretation of a plethora of physical phenomena under thermodynamic equilibria as well as in nonequilibrium dynamic systems.

In this chapter attention is focused on the effects of layered nanofiller particles on the free volume in molten and glassy polymers. Recent rigorous analyses of the PVT data of polymeric nanocomposites (PNCs) using the Simha–Somcynsky (S-S) equation of state has led to better understanding of these new materials. PNCs are composed of a polymeric matrix with dispersed nanoparticles (e.g., platelets, fibers, spheroids) with at least one dimension ≤ 2 nm [Utracki, 2004, 2007b; Okada and Usuki, 2006]. PNCs with all three types of nanoparticles have been prepared [e.g., polyamide with clay, polycarbonate with carbon nanotubes (CNTs), and polystyrene with gold particles], but only PNCs with natural or synthetic layered nanofiller [e.g., clay-containing PNCs (CPNCs)] are commercially available for high-volume structural applications.

Originally, polyamide (PA)-based CPNCs were developed by Toyota and Unitika for the automotive industry. The first description of CPNCs is from 1985, followed by its industrial application four years later [Okada and Usuki, 2006]. Nowadays, CPNCs are used in a number of industries, from transport to packaging, sports equipment, building and construction, electronics and electrical, household and personal care goods, medical and industrial equipment, aerospace and defense [Utracki, 2008b]. The global market share of CPNCs is expected to reach about \$211 million in 2008 [Goliath Business Knowledge, 2006]. A more recent report states that the nanoparticles in the world composites market earned revenues of \$33.7 million in 2006 and is to reach \$144.6 million in 2013 [Frost & Sullivan, 2008]. The exponential growth of all nanocomposites is illustrated by the string of numbers from the German market (year/million, US dollars): 2000/2, 2003/54, 2008/230, 213/860, and 2020/4,690 [Lakoma, 2005].

The CPNC performance depends on the degree of platelets dispersion, with some properties more affected by it (e.g., mechanical, barrier) than others. The degree of dispersion is controlled by the thermodynamic miscibility between polymer and organoclay, solidification of organics on the clay platelets, and their concentration [Utracki, 2004, 2008a]. The PVT measurements and interpretation of the CPNC behavior provide a direct means of extracting information about matrix–clay

interactions, the extent of solidification, and for determining how much the addition of clay platelets affects the matrix free volume, hence the material's performance and properties.

14.1.2 Pressure–Volume–Temperature Measurements

The customary use of *PVT* data has been to determine compressibility, κ , and the thermal expansion coefficient, α , essential in polymer engineering:

$$\begin{aligned} \text{Melt : } \quad \kappa &\equiv -(\partial \ln V / \partial P)_T, \quad \alpha \equiv (\partial \ln V / \partial T)_P \\ \text{Glass and solid : } \quad \kappa &\equiv -(\partial \ln V / \partial P)_{T, P^0, q}, \quad \alpha \equiv (\partial \ln V / \partial T)_{P, T^0, q} \end{aligned} \quad (14.1)$$

Equation (14.1) provides a general definition of the two derivatives for melt, glass, and solidified semicrystalline polymers. In the melt the molecular relaxations are so much faster than the change of the independent variables, q , that it becomes irrelevant, and the customary definitions for κ or α specify only constant T or P , respectively. However, in the nonequilibrium vitreous or semicrystalline systems the properties depend critically on the method of preparation, on P , T , q , and on the vitrification method. Accordingly, the forming pressure and temperature, P^0 and T^0 , and the cooling or compressing rate, q , should be specified [Utracki, 2007a].

Because of the acknowledged thermodynamic equilibrium of fluids, including molten polymers, *PVT* studies focused on melts. The studies not only collect information on the influence of P and T on the specific volume, density, compressibility, and other derivative properties, but in addition, using an adequate theory, they offer an insight into segmental interactions, segmental packing, the free volume, which in turn affects a host of properties, including thermodynamic equilibrium and nonequilibrium properties, such as cohesive energy density, solubility, viscosity, diffusivity, as well as the solid-state performance (i.e., physical aging, crystallization kinetics, etc.). For binary systems the *PVT* data analysis yields information about interactions between constituents: the polymeric matrix and entities dispersed in it: gas bubbles [Xie et al., 1992; Higuchi and Simha, 1996; Xie and Simha, 1997; Simha and Xie, 1998; Simha and Moulinié, 2000; Utracki and Simha, 2001b; Li et al., 2008], domains of immiscible polymers [Zoller and Hoehn, 1982; Jain et al., 1982; Simha and Jain, 1984; Maier et al., 1994; Srithawatpong et al., 1999; Utracki and Simha, 2001a], filler particles [Simha and Jain, 1982; Simha et al., 1982, 1984, 1986; Papazoglou et al., 1989; Simha et al., 1989], or nanoparticles [Simha et al., 2001; Utracki et al., 2003; Nelson et al., 2004; Utracki and Simha, 2004; Bamji et al., 2005].

As discussed in Chapter 6, several equations of states have been proposed for molten polymers, and these have been critically reviewed [Curro, 1974; Zoller, 1989; Rodgers, 1993; Rudolf et al., 1995, 1996; Lambert et al., 2000]. The reviews evaluated the capability of individual equations of state to fit the liquid *PVT* data. However, rigorous analyses of polymer *PVT* behavior in the vitreous state are rare, as the thermodynamic history and time-dependent glass structures complicate the

experiments and their interpretation [Zoller and Walsh, 1995]. Thus, the publications have focused either on molten systems or on glassy amorphous polymers. In this chapter the effects of organoclay addition on *PVT* behavior is analyzed in four parts: (1) the molten polymeric matrix, (2) CPNC in the molten state, (3) the glass transition region, and (4) the vitreous state. In addition, the differences between CPNC behavior with amorphous and semicrystalline polymer will be indicated.

14.2 THEORY

14.2.1 Molten State

Since Chapter 6 presents detailed discussion of Simha–Somcynsky lattice–hole theory, only an outline is provided here. The theory was derived for spherical and chain molecule fluids [Simha and Somcynsky, 1969; Somcynsky and Simha, 1971]. The model lattice contains a volume fraction y of occupied sites and $h = 1 - y$ of nonoccupied sites, or “holes.” From the Helmholtz free energy, F , the S-S equation of state was obtained in the form of coupled equations:

$$\frac{\tilde{P}\tilde{V}}{\tilde{T}} = (1 - \eta)^{-1} + \frac{2y(AQ^4 - BQ^2)}{\tilde{T}} \quad (14.2)$$

$$3c \left[\frac{\eta - 1/3}{1 - \eta} - \frac{y(3AQ^4 - 2BQ^2)}{6\tilde{T}} \right] + (1 - s) - \frac{s}{y} \ln(1 - y) = 0 \quad (14.3)$$

where $Q = 1/(y\tilde{V})$, $\eta = 2^{-1/6}yQP^{1/3}$, and $A = 1.011$ and $B = 1.2045$ are coefficients, which account for the nearest-neighbor interaction centers in the face-centered cubic lattice (fcc). Since the derivation of Eq. (14.3) implicitly involved the thermodynamic equilibrium, it may be utilized in the analysis of liquids but not of glasses.

In the relations above, the variables marked with a tilde are reduced, defined in terms of the Lennard-Jones (L-J) maximum attractive energy, ε^* , and the segmental repulsion volume, v^* , per statistical segment. The statistical segment is defined as $M_s = M_n/s$ where M_n is the number-average molecular weight and s is the number of macromolecular segments, statistically often corresponding to the number of carbon atoms in the backbone chain:

$$\left. \begin{aligned} \tilde{P} &= \frac{P}{P^*}, & P^* &= \frac{zq\varepsilon^*}{sv^*} \\ \tilde{T} &= \frac{T}{T^*}, & T^* &= \frac{zq\varepsilon^*}{Rc} \\ \tilde{V} &= \frac{V}{V^*}, & V^* &= \frac{v^*}{M_s} \end{aligned} \right\} \frac{P^*V^*}{RT^*} M_s = \frac{c}{s} \quad (14.4)$$

where the parameter $3c$ indicates the external volume-dependent degrees of freedom, R is the gas constant [$R = 8.31447$ (J/K·mol)], and $zq = s(z-2) + 2$ is the number of interchain contacts [z is the lattice coordination number ($z = 12$ for hexagonal close-packed or face-centered cubic structures)]. The coupled equations (14.2) and (14.3) describe the PVT liquid surface and the free-volume quantity associated with it, $h = h(\tilde{V}, \tilde{T})$. Fitting these to PVT data leads to a set of P^* , T^* , V^* -reducing parameters. For linear polymers with $3c/s = 1 + 3/s \approx 1$, the L-J parameters might be calculated as ε^* (kJ/mol) $\approx RT^*/30 = 2.771T^*$ and v^* (mL/mol) $= V^*M_s$.

Assuming random mixing, Jain and Simha [1980, 1984] have shown that in binary systems, Eqs. (14.2) and (14.3) retain validity, but the L-J parameters ε^* and v^* are compositional averages of 11, 22, and 12 interactions:

$$\langle \varepsilon^* \rangle \langle v^* \rangle^p = X_1^2 \varepsilon_{11}^* v_{11}^{*p} + 2X_1 X_2 \varepsilon_{12}^* v_{12}^{*p} + X_2^2 \varepsilon_{22}^* v_{22}^{*p}; \quad p \in [2, 4] \quad (14.5)$$

where the site fractions, X_1 and $X_2 = 1 - X_1$, are functions of the mole fractions $x_1 = 1 - x_2$:

$$X_1 = \frac{q_1 z x_1}{q_1 z x_1 + q_2 z x_2}; \quad X_2 = 1 - X_1 \quad (14.6)$$

Accordingly, CPNCs might be treated as a binary mixture of a matrix (index 1) with dispersed solid particles (index 2). Evidently, CPNCs are more complex, comprising polymer, inorganic intercalated particles, excess intercalant, compatibilizer(s), and a diversity of industrial additives. Furthermore, there is a great variety in the ways in which the inorganic platelets interact with the organics, affecting the degree of dispersion. For example, in reactively prepared CPNC with polyamide-6 (PA-6) as the matrix, clay platelets are exfoliated and each of them is ion-bonded to thousands of PA macromolecules. Flow analysis of such CPNCs (e.g., Ube 1015C2 hybrid) led to the model of hairy clay particles (HCPs) dispersed in a polymeric matrix [Utracki and Lyngaae-Jørgensen, 2002]. Because of the polarity of PAs and strong interaction with negatively charged clay platelets, PA-based CPNCs are relatively easily prepared with a high degree of exfoliation. Contrast these systems with those having a nonpolar matrix, such as polyolefin (PO), or polystyrene (PS), which do not bond to a clay surface and in addition are immiscible with the customarily used paraffinic intercalant; in these systems a functional compatibilizer is required. In consequence, before defining what constitutes phase 1 and phase 2, information regarding composition, thermodynamic interactions, and resulting degree of dispersion is required for converting the physical system into a two-component model.

Solidification on a high-energy solid surface has been observed using a surface force analyzer (SFA) [Israelachvili et al., 1984; Horn and Israelachvili, 1988] and the neutron scattering method [Cosgrove et al., 1987, 1991]. The presence of a solidified layer has been predicted by the molecular dynamics (MD) or Monte Carlo (MC) methods [Fleer et al., 1993; Hentschke, 1997; Termonia, 2009]. The information indicates that in the orthogonal (to the clay surface) direction, between the clay surface and the liquid matrix (with “bulk properties,” i.e., expected molecular mobility at given

T and P), there are two layers with reduced molecular dynamics: (1) a solid layer of organic molecules, $z_1 \approx 2$ to 9 nm thick, and (2) a layer where the molecular mobility increases progressively from z_1 to $z_2 \approx 100$ to 120 nm. The behavior is general, observed for low- and high-molecular-weight organic liquids, but the limits depend on the molecular weight of the interacting organic and its affinity to the nanoparticle surface [Hu and Granick, 1992]. Experiments by Luengo et al. [1997] demonstrated that polybutadiene (PBD; weight-average molecular weight $M_w = 6.95$ kg/mol) on freshly cleaved mica flakes had $z_1 \approx 5$ to 6 nm and $z_2 \approx 100$ nm; only above the latter limit did the rheological data in steady-state and dynamic shearing show the expected PBD “bulk flow” behavior.

Consequently, the basic model of CPNCs assumes that solid particles are made of clay platelets or their stacks covered with a z_1 -thick, solidified organic layer (intercalant, compatibilizer, and/or polymer), while the matrix comprises the remaining liquid materials, including the second layer of the organics at $z > z_1$ having variable molecular mobility. Thus, in CPNCs the second component (with interaction parameters ε_{22}^* and v_{22}^*) is the clay platelet encased in a $z_1 \approx 4$ - to 6-nm-thick layer of organic molecules, while the first one (with ε_{11}^* and v_{11}^*) is the matrix away from the clay surface at $z > z_1$. Consequently, the matrix containing molten polymer, with it, excess intercalant, compatibilizer(s), and standard industrial additives dissolved or dispersed in it, may not be homogeneous, and certainly its molecular mobility varies with distance from the clay surface at $z > z_1$. It is expected that this model will lead to clay content-dependent ε_{11}^* and v_{11}^* values. However, this variability is limited to relatively low clay concentration, below the limiting value at which the molten polymer with the bulk properties disappears and clay platelets are dispersed within the second layer, where the chain mobility depends on the distance from the clay surface, $z_1 < z < z_2$.

To describe the variation of L-J parameters with distance from the clay surface, $\varepsilon_{ij}^*(z)$ or $v_{ij}^*(z)$, an exponential function was adopted [Utracki and Simha, 2004]:

$$y(z) = \frac{y_1 y_2}{y_1 - (y_1 - y_2) \exp \left\{ n \left[(z - z_1) / (z - z_2) \right] \right\}}; \quad (14.7)$$

$$z_1 \leq z < z_2; \quad y \in [\varepsilon^*, v^*]$$

where n is an adjustable parameter and y_1 represents the L-J parameters at the solidified polymer layer at z_1 . For large values of $z \leq z_2$ the exponential term becomes negligible compared to y_1 and y approaches a constant value of y_2 , characteristic for the bulk polymer. Thus, at the lower limit, $y(z) = y_1$ becomes $\varepsilon^*(z) = \varepsilon_{22}^*$ and $v^*(z) = v_{22}^*$, while for the upper, the characteristic values of the matrix are obtained: $\varepsilon^*(z) = \varepsilon_{11}^*$ and $v^*(z) = v_{11}^*$. An example of calculations of the L-J binary interaction parameters from Eqs. (14.5)–(14.7) is provided in Section 14.4.4.

In CPNCs there are three limiting clay concentrations:

1. The maximum concentration for clay exfoliation, ϕ_{\max}
2. The concentration at which free matrix with bulk properties disappears, ϕ_1 (i.e., the concentration above which only clay platelets with two layers of reduced mobility are present)

3. The concentration at which clay platelet with the solidified layer of organics is left, ϕ_2

To calculate these concentrations, two models may be used: model 1, of a well-dispersed system, such as PA-6-based CPNC, and model 2, of a nonexfoliated system, such as PS-based CPNC. The clay platelets will be assumed to be single-size flat disks with diameter $d = 280$ nm and thickness $t = 1$ nm. These dimensions correspond to those of montmorillonite (MMT) present in commercial organoclays (measurements of individual MMT platelets gave the weight-average dimensions: length/width/thickness = 350/219/1.0 nm).

Model System 1 The exfoliated clay platelets are encased in a 6-nm-thick layer of solidified organic phase. The platelets remain exfoliated up the limiting concentration, where the crowding prevents free rotation; thus, $\phi_{\max} = 0.62$ for the encompassed volume of clay platelet, or expressing the encompassed volume in terms of actual dimensions: $\phi_{\max} = 0.62[3(t + 2z_1)]/[2(d + 2z_1)] \approx 0.0414$, which corresponds to $w_{\max} \approx 0.86$ wt% of inorganic content. Above this first limiting concentration, the clay platelets must form stacks, with the interlayer thickness decreasing with clay loading. The stacks are made of clay platelets (thickness = t) and organic phase (thickness = $2z$); thus, $z = (t/2)(1/\phi - 1)$. Accordingly, $\phi_1 = 0.0051$ and $\phi_2 = 0.111$, or expressing it again in wt% of inorganic phase, $w_1 = 1.32$ and $w_2 = 24.5$ wt%.

Model System 2 The transmission electron microscopy (TEM) of highly diluted PS-based CPNCs shows the presence of individual platelets and stacks. However, as clay concentration increases, the individual platelets disappear and only stacks are evident [Tanoue et al., 2004a,b, 2005]. According to x-ray diffraction (XRD), the interlayer spacing within the stacks was $d_{001} \approx 1.4$ nm and the average number of clay platelets was 6. The second model is assumed to be composed of identical, slightly displaced circular stacks with diameter $d = 280 + 2z_1$ (nm), thickness $t = 11.4 + 2z_1$ (nm), where for this system with weak clay-polymer interactions, $z_1 = 4$ nm might be used. The expression $\phi_{\max} = 0.62[3(t + 2z_1)]/[2(d + 2z_1)]$ may be used for calculating the concentration at which stacks will stop rotating (i.e., $\phi_{\max} = 0.0413$ or $w_{\max} \approx 1.99$ wt% of inorganic content). Similarly, treating these compact stacks as individual particles, one may express the distance between two stacks as $2z = (tV/V_{\text{clay}})(100/w - 1)$ [Utracki, 2004]. Since the stacks are never perfectly aligned, their aspect ratio may be small (i.e., $p \geq 288/19 \approx 15$). Thus, they are thick disks covered by a layer of solidified organics, significantly more sluggish than individual platelets in model system 1. As a consequence, they may form percolated, rigid structures at relatively low concentrations. For prolate and oblate ellipsoids a Padé-type expression between the percolation threshold, ϕ_p , and the aspect ratio, p , has been proposed [Garboczi et al., 1995]:

$$\phi_p = \frac{sp + p^2}{a + bp + cp^{3/2} + dp^2 + ep^3} \quad (14.8)$$

with $s = 9.875$, $a = 7.742$, $b = 14.61$, $c = 12.33$, $d = 1.763$, and $e = 1.658$. For $p = 15$, Eq. (14.8) gives $\phi_p \leq 0.060$, which corresponds to $w_1 \geq 3.1$ wt% of inorganic clay; this value is not far from the experimental $w_{\text{crit}} \geq 3.6$ wt% MMT found for a series of PS-based CPNCs [Utracki, 2008c].

Support for the idea of a percolated structure connected by solid bridges may be found in the Frisk and Laurent [1996] patent on the reduction of permeability through a polyester wall container; reduction by a factor of 100 was reported after addition of $w = 5$ wt% clay (aspect ratio $p = 1000$ to 1500). This large effect cannot be explained by the standard mechanism of tortuosity [see Utracki, 2004, vol. 2], but it is logical if combined with the intrinsic reduction of matrix permeability caused by solidification of polymer on clay platelets that form a continuous barrier to CO_2 flux.

14.2.2 Glass and Other Transitions

The glass transition temperature (T_g) separates the vitreous from the molten state; it is a freezing–unfreezing temperature of micro-Brownian motion involving 20 to 50 carbon atoms of the main chain [Boyer, 1977, 1980, 1985, 1987]. The more recent twinkling fractal theory (TFT) postulates that upon cooling of a molten polymer, dynamic percolating fractal structures are formed [Wool, 2008a,b; Wool and Campanella, 2009]. The solidlike aggregates reach the percolation threshold at T_g ; thus, the transition from melt to glass is controlled by critical percolation (i.e., segmental interactions, dimensionality, and aspect ratio), as well as the packing arrangement (i.e., by the thermodynamics, kinetics, and segmental geometry). Accordingly, T_g represents a percolation threshold of the transition region structures formed in a wide range of independent variables [Utracki, 2009c].

The experimental value of T_g and its functional relationships might depend on the test method; for example, for nitrile rubber (NBR)/organoclay, differential scanning calorimetry (DSC) gave a composition-independent value of $T_g = 248$ K, while PALS showed that T_g increases with clay loading from 237 to 252 K [Kim et al., 2007]. A similar disagreement was observed for the melting point of PA-6-based CPNC: DSC showed T_m to be independent of clay content, whereas PVT indicated its value increasing with solid loading [Utracki, 2009a,b].

Being kinetic in nature, T_g depends on the cooling or compressing rate, q , as well as on P^0 during cooling or T^0 during compressing [i.e., Eq. (14.1)]. Thus, each substance vitrifies into a spectrum of glasses with different structures and physical aging kinetics [Cowie et al., 2002]. It has been expected that the T_g value obtained by extrapolation to infinite measurement time represents the characteristic parameter of a given substance, independent of the method of determination [Mercier and Aklonis, 1971]. Pragmatically, the pseudoequilibrium T_g values tabulated in handbooks have been either measured at $q \leq 0.01$ K/s, or extrapolated to the temperature at which the zero-shear viscosity $\eta_0 \approx 10^{12}$ Pa·s.

In analogy to the Ehrenfest derivation, from $f(T, P, h) = 0$, Quach and Simha [1971, 1972] obtained a general expression for the P dependence of T_g :

$$\frac{dT_g}{dP} \cong \frac{\Delta\kappa}{\Delta\alpha} + \left(\frac{\partial T}{\partial h} \right)_p \frac{dh_g}{dP} \quad (14.9)$$

where $dh_g/dP = dh(T_g, P_g)/dP$ and $(\partial T/\partial h)_P$ is computed from isobaric data in the molten state near T_g [McKinney and Simha, 1974]. From Eq. (14.9) the Ehrenfest relation for the second-order phase transition is recovered if $dh/dP = 0$ (i.e., when the liquid disorder near T_g is independent of pressure):

$$\frac{dT_g}{dP} = \frac{\Delta\kappa}{\Delta\alpha} = \left(\frac{dT}{dP}\right)_h^l \quad (14.10)$$

where Δ specifies a difference between values for the liquid and glass, and the superscript l indicates liquid. The latter relation is expected to be valid for the low-pressure glasses (LPGs) formed by melt cooling below T_g at ambient pressure (the glass formed by pressurizing melt is called high-pressure glass) [Quach and Simha, 1972; Zoller, 1978; Schmidt, 2000].

In amorphous polymers T_g is the main transition, with several weaker ones in the glassy and molten states, usually too feeble to be evident on the PVT surface, but seen in the derivative properties and in spectroscopy. For example, at $T < T_g$ there are several glass–glass transitions, of which $T_\beta \approx 0.76T_g$, is nearest to T_g . According to Struik [1978], the rate of physical aging is zero at T_β and T_g , reaching maximum about halfway between these two (i.e., $T_{\max} \approx 0.88T_g$). Similarly, at $T > T_g$ there are several transitions, of which the one at $T_T/T_g \approx 1.2 \pm 0.1$ is the easiest to detect [Utracki, 2007a]. Coincidentally, within these limits, Boyer [1977, 1980, 1985, 1987] postulated the presence of a liquid–liquid transition temperature, T_{LL} . Other mechanisms based on molecular modeling and/or NMR measurements postulate the existence of the crossover transition temperature, $T_c/T_g \approx 1.2 \pm 0.1$, separating the regions of structural and segmental relaxations where liquid exists as an assembly of particles enclosed in cages formed by their neighbors [i.e., mode-coupling theory (MCT)] [Götze and Sjögren, 1988; Kisliuk et al., 2000; Paul, 2004; Casalini and Roland, 2005]. Ngai [2000, 2003] extended the MCT to cooperative relaxation systems. The temperature dependence of the relaxation time or viscosity in the melt was found to follow two Vogel–Fulcher–Tammann–Hesse (VFTH) dependencies:

$$\log t(T) = A + \frac{B}{T - T_0} \quad (14.11)$$

intersecting at $T_B \approx T_c$. At high temperature the VFTH intersects the Arrhenius equation at $T_A \approx 1.8T_g$. In Eq. (14.11), A , B , and T_0 are constants, the latter frequently being equated with the Kauzmann temperature, T_K , at which the configurational entropy vanishes. Again, on the PVT plot there is no evidence of the macroscopic transition at $T_B > T_g > T_0 \approx T_g - 50$. The transition at $T_B \approx T_c$ has been postulated to originate in the fast vibrations of macromolecular backbone or its side-group motion, which starts at the temperature in the glassy state and stretches to $T > T_c$. In macromolecular liquids another mechanism, the elementary relaxations related to conformational transitions, also extends to temperatures well above T_c . According to TFT, the dynamic percolating fractal structures form at $T_c > T(K) > 0$ [Wool, 2008a,b].

14.2.3 The Vitreous State

From the Helmholtz free energy, written as a function of the specific volume, temperature, and occupied lattice site fraction, $\tilde{F} = \tilde{F}[\tilde{V}, \tilde{T}; y(\tilde{V}, \tilde{T})]$, the pressure is derived as [McKinney and Simha, 1974, 1976, 1977]

$$-\tilde{P} = \left(\frac{\partial \tilde{F}}{\partial \tilde{V}} \right)_{\tilde{T}, y} + \left(\frac{\partial \tilde{F}}{\partial y} \right)_{\tilde{V}, \tilde{T}} \left(\frac{\partial y}{\partial \tilde{V}} \right)_{\tilde{T}} \quad (14.12)$$

For systems at thermodynamic equilibrium, the derivative $(\partial \tilde{F} / \partial y)_{\tilde{V}, \tilde{T}} = 0$ and Eq. (14.12) reduces to the classical expression $\tilde{P} = -(\partial \tilde{F} / \partial \tilde{V})_{\tilde{T}, y}$, used for deriving Eq. (14.2). However, for vitrified systems, the full Eq. (14.12) should be used. McKinney and Simha solved the relation numerically and compared the results with those obtained from Eq. (14.2) only (called the *simplified* procedure). The computations indicated that the trends for all functions were similar and that the numerical differences were comparable to the experimental errors. For example, the hole fraction computed from Eq. (14.12) was smaller by 2 to 6% than that calculated from Eq. (14.2). Thus, the simplified procedure may be used for analyses of vitreous-state *PVT* data.

The simplified procedure starts with computation of the characteristic P^* , T^* , V^* parameters from the *PVT* data at $T > T_g$. Next, from Eqs. (14.2) and (14.3), the fictitious hole fraction in the glassy state at $T' < T_g$ and P' (a prime indicates an independent variable in the vitreous state) is calculated as $h_{\text{extrapol}} = h(T', P')$. Subsequently, from the *PVT* data at $T' < T_g$, using Eq. (14.2), the hole fraction in the glassy state, $h_{\text{glass}} = h(T', P')$, is computed. Thus, for the same set of T' , P' , the hole fractions that the melt would have, h_{extrapol} , and the factual one, $h_{\text{glass}} > h_{\text{extrapol}}$, are determined. From the isobaric values of h versus T' , the frozen fraction of free volume is calculated as [McKinney and Simha, 1974]

$$FF_T = 1 - \frac{(\partial h / \partial T')_{P, \text{glass}}}{(\partial h / \partial T')_{P, \text{extrapol}}} \quad (14.13)$$

The parameter FF_T is the fraction of the free volume trapped by vitrified segments. Consequently, the nonfrozen fraction, $1 - FF_T$, is the main contributor to material behavior in the vitreous state.

14.3 PVT BEHAVIOR AND DERIVATIVES

14.3.1 PVT of Amorphous Polymers and Their CPNCs

The $V = V(P, T)$ dependence is measured in a pressure dilatometer usually within the range of temperatures from ambient to about 700 K, and pressures from 10 to 200 MPa in steps of $\Delta T = 5$ or 10°C and $\Delta P = 10$ to 30 MPa. The zero-pressure value is obtained by extrapolation of data measured between 10 and 30 MPa (in 1-MPa steps)

using the Tait relation, Eq. (6.10). Prior to testing, the material is dried (e.g., polyamide for 48 hours at 80°C). Since the instrument measures only the incremental changes in the specific volume, $\Delta V = \Delta V(P, T)$, the value of specific volume under ambient conditions must be measured with an accuracy of $\Delta V \leq \pm 0.001 \text{ mL/g}$. Considering the high hygroscopicity of some polymers, all manipulations ought to be performed in a glove box under a positive pressure of dry N_2 . Owing to the low clay content (i.e., small volume changes), each sample should be tested at least twice.

There are two testing strategies: isobaric and isothermal. In the former, at each level of pressure the volume changes over the full range of temperature are carried out, then P is adjusted to the next level and the process is repeated. Similarly, during the isothermal runs the temperature is set and $V = V(P)_T$ is determined, then T is changed and the process is repeated. Furthermore, the tests might be carried out starting at ambient T and increasing it to maximum, or the reverse, starting at high T and decreasing it toward the ambient. As far as the melt behavior is concerned, selection of either one of the four methods is not important: The system is at thermodynamic equilibrium. However, polymers do degrade at high temperatures and it is preferable to expose them to the highest temperature only once, as in the “standard” isothermal mode, with increasing T [Zoller and Walsh, 1995; Simha et al., 2001; Utracki et al., 2003]. The data collected during such runs are displayed in Figure 14.1a. By contrast, when the T_g and vitreous state are of interest, it is more appropriate to start at $T \approx T_g + 30$ and cool the melt isobarically down to the vitreous region. After each isobaric run, the specimen should be reheated to the initial temperature, allowed to relax, and then recompressed [Quach and Simha, 1971]. The problem with this strategy is the relatively small range of T within the molten phase, which reduces the accuracy of the interaction parameters calculated from Eq. (14.4). As a result, most *PVT* tests are conducted following the standard isothermal procedure [Zoller and Hoehn, 1982; Zoller, 1989; Zoller and Walsh, 1995; Schmidt and Maurer, 1998; Han et al., 1999; Utracki, 2007a]. For improved reproducibility, dry samples might be loaded into a dilatometer, premolded internally under vacuum at $T \geq T_g$ or $T \geq T_m$, cooled to room temperature, and then tested following the standard procedure.

The information discussed in this chapter is based mainly on work carried out in the author’s laboratory on several types of CPNCs. Of particular value are the results of standard *PVT* tests on polystyrene (PS)-based CPNC (see Table 14.1). These were prepared by melt-compounding PS with organoclay in a twin-screw extruder (TSE) equipped with a high-stress screw at $T = 200^\circ\text{C}$ with throughput $Q = 5 \text{ kg/h}$. The PS-1301 from Nova had $M_w = 270 \text{ kg/mol}$, melt flow rate $= 3.5 \text{ g/10 min}$, and density $\rho = 1.04 \text{ g/mL}$. The organoclay Cloisite 10A (C10A) from Southern Clay Products, was Wyoming montmorillonite (MMT) preintercalated with 39 wt% of dimethyl benzyl hydrogenated tallow ammonium chloride (2MBHTA). The ingredients’ characteristics, compounding procedure, and properties have been published [Tanoue et al., 2004a,b, 2005]. For comparison of the amorphous with semicrystalline polymer behavior, few results for PA-6-based CPNC will also be presented [Utracki, 2009a,b].

To assess the data accuracy, the tests were repeated two to five times. Furthermore, the effects of the holding time between measurements (from 0 to 90 s) were

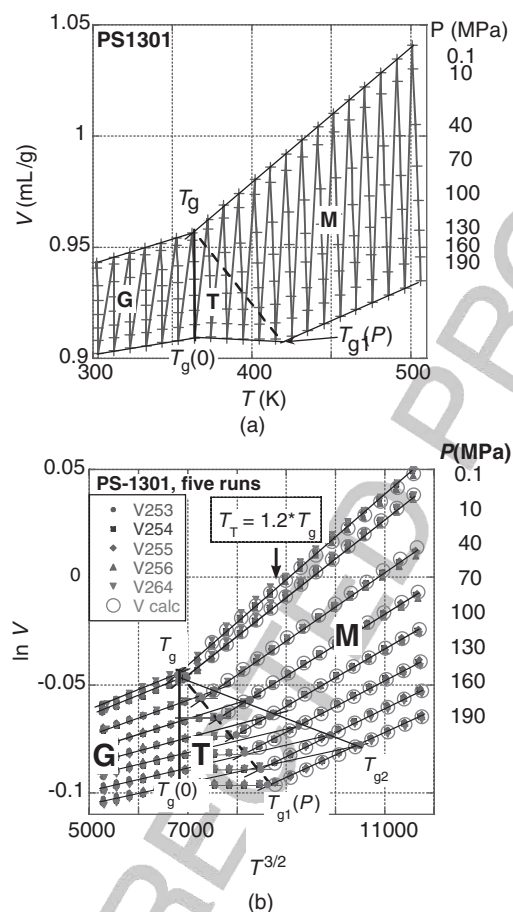


FIGURE 14.1 PVT data for PS-1301 are plotted (a) linearly and (b) as $\ln V$ versus $T^{3/2}$. The straight lines are fitted to data within the glassy and molten regions. **G**, **T**, and **M** indicate the glass, transient, and melt regions, respectively. The **T** region is limited by the vertical solid line, $T_g(0)$, and the dashed line $T_{g1}(P)$. Graph (a) also indicates the “standard” sequence of isothermal measurements; graph (b) presents reproducibility of five consecutive runs.

examined. The total run time was 18 to 32 hours. The average error of measurements for the specific volume (V) was $\leq 0.03\%$. The PVT plots in Figure 14.1 show the PS behavior. The range of the independent variables ($T = 373$ to 517 K and $P = 0.1$ to 190 MPa) extended from below T_β to above T_c (for PS-1301 at $P = 1$ bar the secondary transitions in the glassy and molten states are at $T_\beta \simeq 290$ to 310 K and $T_T \simeq 420$ to 440 K, respectively), but these transitions are not apparent on the PVT surfaces [Simha et al., 1973]. The data are plotted as isobars in either a V versus T or an $\ln V$ versus $T^{3/2}$ plot. The linear plot is more familiar, and within a narrow range of variables it is often adequate for data linearization within the molten and glassy

TABLE 14.1 PS-Based CPNC: Composition and Properties

No.	Code	CPNC ^a	MMT (wt%) ^b	V (mL/g) ^c	d_{001} (nm) ^d	M^e
0	C10A organoclay	—	61	—	1.93	
1	HS16	PS	0	0.93710		
2	HS16A	PNC-1	1.4	0.93251	4.9	3.3
3	HS17	PNC-2	2.8	0.92793		
4	HS18	PNC-5	5.7	0.91843	4.02	3.7
5	HS19	PNC-10	10.6	0.90237	4.18	3.3
6	HS20	PNC-17	17.1	0.88108		

Source: Data from Tanoue et al., [2004a,b, 2005].

^aSample code used in the text.

^bInorganic MMT content.

^cSpecific volume at $T=516.84$ K and $P=190$ MPa; V decreases with clay loading with a slope of -0.003276 .

^dInterlayer spacing from XRD.

^eNumber of clay platelets in a stack (peak 1).

regions. Figure 14.1a shows the sequence of data collection during the standard test procedure. Thus, the measurements start at the lowest T and P (left top point) and follow to the highest T and P (right low point). The transient region (T) is bordered by the vertical straight line $T_g(0)$ and the dashed $T_{g1}(P)$ line. The origin of the latter plot goes to early observations by Bueche [1962], and it has been used by Simha and his colleagues for linearization of the V - T data at $P=0$, and then extraction of the reducing parameters V^* and T^* [Simha et al., 1973; Utracki and Simha, 2001]. The graph shows data reproducibility. Qualitatively, there is no difference between the two methods of plotting. In addition, Figure 14.1 also illustrates the two methods of T_g evaluation: T_{g1} represents the boundary temperature between the melt and transient region, whereas T_{g2} represents that at which the lines fitted to isobaric V - T data in the molten (M) and glassy (G) regions intersect. The former method evolved from the customary analysis of the PVT data, and it has commonly been used [Zoller and Walsh, 1995; Simha et al., 2001; Utracki and Simha, 2003; Utracki et al., 2003]. The latter procedure was originally suggested by Kovacs but seldom used [Kovacs, 1958; Kovacs and Hutchinson, 1979; Zoller, 1978]. Evidently, for the ambient P the two methods are equivalent, $T_{g1} = T_{g2}$, but as P and organoclay content increase, the transient region makes the second method objectionable. This is evident in Figure 14.2, where data at $P=190$ MPa for three clay concentrations are shown. Because of solidification of molten PS on the clay surface on cooling CPNCs from high temperature, a large free-volume fraction is frozen; thus, reheating it from below T_β the glass may shrink; the presence of T_{g2} in the G-region invalidates the T_{g2} estimation. It is noteworthy that T_β increases with P : $T_\beta(\text{K}) = T_{\beta 0} + 0.21P \text{ MPa}$ [Eisenberg and Shen, 1970; Zoller, 1978]. As Figure 14.3 shows, T_{g1} determined from PVT plots is consistent with the DSC results. Consequently, only the results of the first method, $T_{g1}(P)$, will be used.

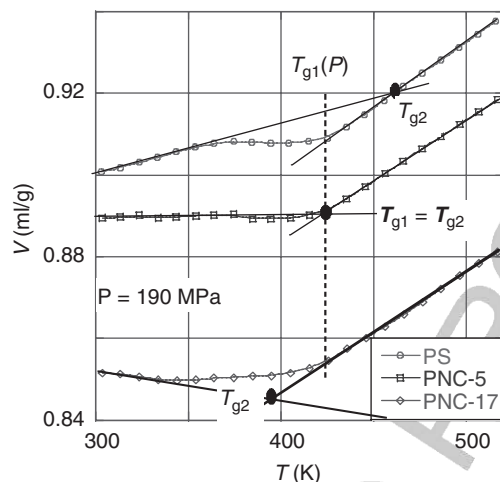


FIGURE 14.2 Specific volume versus T at $P = 190$ MPa for PS and CPNC containing 5.7 and 17.1 wt% MMT. At this pressure, $T_{g1}(P)$ is independent of the MMT content. The error of the measurements is smaller than the data points.

The degree of clay dispersion in a PS matrix was characterized by x-ray diffraction analysis (XRD), and electron microscopy: that is, scanning [with field emission gun scanning electron microscopy (FEGSEM)] and transmission (TEM); the results are listed in Table 14.1. The XRD scans were obtained at a scan rate $0.3^\circ/\text{min}$. The specimens were prepared by compression molding at $T = 200^\circ\text{C}$ and a compressive

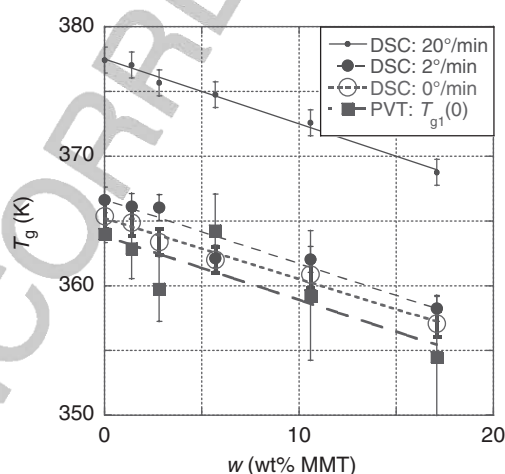


FIGURE 14.3 Glass transition temperatures versus clay content for PS and its CPNC. Results from PVT at $P = 0.1$ MPa and from DSC at scan rates 20 and 2, extrapolated to $0^\circ\text{C}/\text{min}$. The DSC error for T_g is $\pm 1^\circ\text{C}$.

force of 5 tons followed by re-molding on a cleaned glass slide to improve accuracy. The interlayer spacing was calculated from the XRD main diffraction peak position using Bragg's formula:

$$d_{00n} = \frac{n\lambda}{2 \sin \theta} \quad (14.14)$$

where n is an integer, θ is the angle of x-ray beam incidence, and λ is the x-ray wavelength. The thickness of the diffracting stack, t , was calculated from peak broadening [Scherrer, 1918]:

$$t = \frac{k\lambda}{B_{1/2} \cos \theta_B} \quad k \simeq 0.9 \quad (14.15)$$

where $B_{1/2} \simeq \theta_1 - \theta_2$ is peak width at half peak height ($I_{\max}/2$), and $\theta_B \simeq (\theta_1 + \theta_2)/2$. From Eq. (14.15) the number of clay platelets per average stack was calculated as $m = 1 + t/d_{001}$. The electron micrographs confirmed the presence of short clay platelets stacks, deduced from the XRD data [Tanoue et al., 2004a].

14.3.2 PVT of Semicrystalline Polymers and Their CPNCs

Recent analysis of the PVT behavior of PA-6-based CPNCs revealed significant differences between systems having amorphous and semicrystalline matrix. The difference is particularly striking, comparing the region of the main transition: vitrification and crystallization, respectively. The experimental procedure has been the same. The basic characteristics of the PA-6 systems are listed in Table 14.2 [Utracki, 2009a,b].

14.3.3 Compressibility Coefficient, κ

The κ and α coefficients defined in Eq. (14.1) might be calculated directly from the experimental $\ln V$ versus P or T plots, respectively. Examples of the κ versus T plots are presented in Figure 14.4a to c for PS, PNC-2, and PNC-17, respectively. Because of scarcity of data at $T < 320$ K, the initial results and the determination of the T_β were omitted. By contrast, T_g and T_T are visible for all compositions, with

TABLE 14.2 Characteristics of the PA-6 (1022B from Toyota) Samples

Parameter	PA-6	PNC-2	PNC-5
Clay content (wt%)	0	2.29 ± 0.13	4.91 ± 0.24
Interlayer spacing, d_{001} (nm)	—	5.88 ± 0.08	5.62 ± 0.28
Degree of exfoliation (%)	—	93 ± 4	39 ± 16
Number of clay platelets in stacks	—	<2	<3
Melting point, T_m (K)	495 ± 1	485 and 494 ± 1	486 and 494 ± 1
Crystallization temperature, T_c (K)	452 ± 1	461 ± 1	472 ± 1
Crystallinity, X_{cryst} (%)	36 ± 3	30 ± 1	26 ± 1

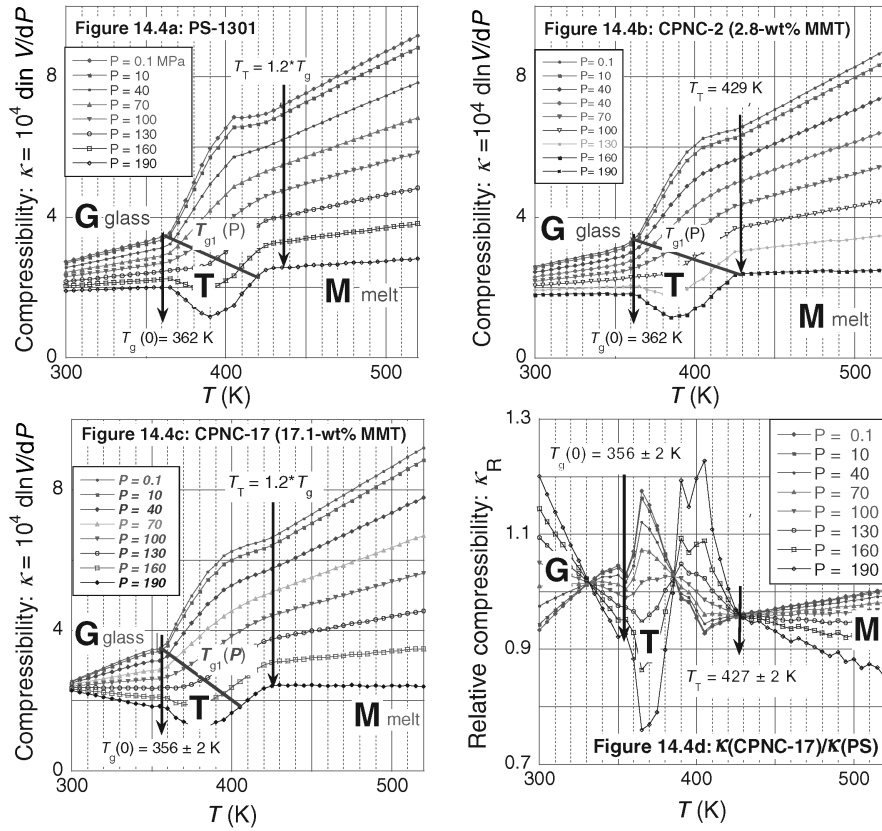


FIGURE 14.4 Compressibility and relative compressibility for PS, PNC-2, and PNC-17 containing $w = 0, 2.8$, and 17.1 wt% MMT, respectively; see the text.

$T_T/T_g \approx 1.2 \pm 0.1$ (note in Figure 14.1 that V increased with T without a discernible change of slope at T_T). The clay mainly affects the vitreous region where the temperature gradient, dk/dT , decreases with increasing P and clay content to negative values (e.g., for PNC-17). To better illustrate the clay effects, the relative compressibility

$$\kappa_R \equiv \left. \frac{\kappa_{\text{CPNC}}(T)}{\kappa_{\text{PS}}(T)} \right|_P \quad (14.16)$$

is displayed in Figure 14.4d. Evidently, the effect is not limited to the glassy region, **G**, but it affects the transitory and molten regions as well. The transition at T_T is now

a cusp, above which κ vary linearly with T ; at low P , the κ of PNC-17 increases faster than that of PS, whereas at high P the reverse is true. The origin of the two other cusps at lower temperatures is uncertain; however, they are not related to the “calorimetric” T_g nor to T_β . Indeed, $T_g(P)$, marked in Figure 14.4a to c by a solid line with a negative slope, cuts across the middle of the transient-T region instead of being a boundary of it as in Figure 14.1.

It is important to recognize that the transition at T_T is also evident in the plots of κ versus T of PS-686 [Quach and Simha, 1971]: $T_T = 447$ K (i.e., $T_T/T_g = 1.22$); PS-Z110 [Zoller and Walsh, 1995]: $T_T = 450$ K (i.e., $T_T/T_g = 1.23$), or other homopolymers—the behavior is general. Thus, in the vicinity of the glass transition in amorphous polymers and their CPNCs there is a large transitory zone of variable structure and properties where with decreasing T and/or increasing P there is formation of dynamic fractal solid structures; the true liquid behavior may be expected only at higher temperatures, $T > T_T$ [Wool, 2008a].

14.3.4 Thermal Expansion Coefficient, α

Slopes of the isobaric lines in Figure 14.1 are constant within the **G** and **M** regions, and variable within **T**. Accordingly, the thermal expansion coefficient, $\alpha = \alpha(T)$, of PS (and PNC-1), shows the expected behavior: constant and nearly P -independent values in the vitreous phase, a short transient zone, and then again constancy in the melts, its value decreasing with increasing P [Briatico-Vangosa and Rink, 2005]. For PNC-17 containing a large quantity of MMT, the plot of α versus T in Figure 14.5 resembles the CPNC κ -behavior shown in Figure 14.4c. However, at low T the values of α are negative instead of positive and constant. Similar dependencies were found for the other CPNC samples with $w > 2.8$ wt% MMT.

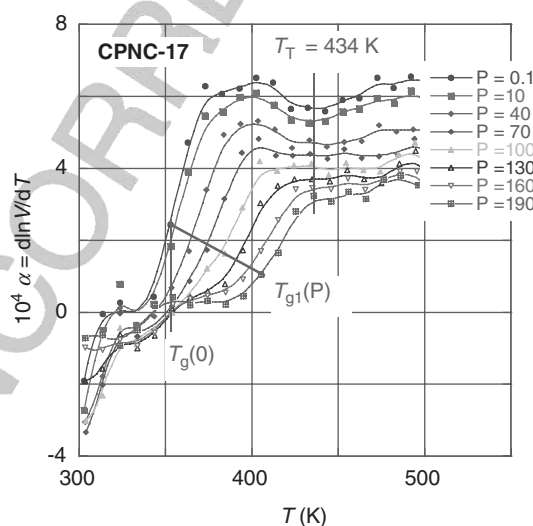


FIGURE 14.5 Temperature dependence of the thermal expansion coefficient, α , for PNC-17.

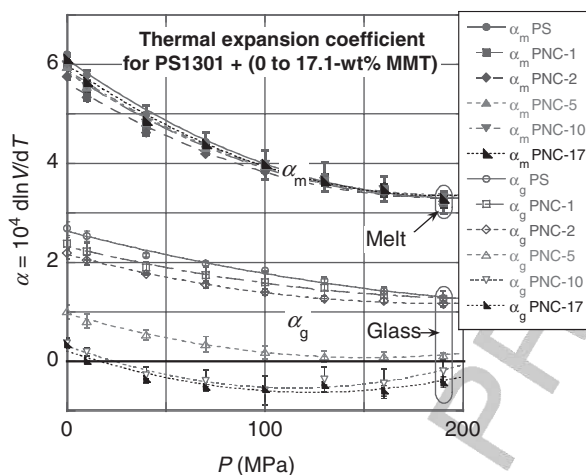


FIGURE 14.6 Pressure dependence of the thermal expansion coefficient for PS-1301 and its CPNC in the glassy, α_g , and molten, α_m , regions.

Comparing the dependencies in Figure 14.4 with those in Figure 14.5 shows that the experimental error for α is larger than that for κ . The former coefficient was calculated from the $\ln V$ versus T plot of experimental data using three different five-point moving arch procedures, averaged in the figure. The difference in the error originates in the test method; that is, at constant T , precisely adjusting P , while allowing for small variations of T during the adiabatic heating. The variation is slight, but evident, in the derivative properties.

The pressure dependencies $\kappa = \kappa(P)$ and $\alpha = \alpha(P)$ are less informative than their temperature equivalents: $\kappa = \kappa(T)$ and $\alpha = \alpha(T)$. This is illustrated in Figure 14.6, displaying $\alpha = \alpha(P)$ in molten and vitreous states for all CPNCs. For homopolymers, α dependence on P is well approximated by a second-order polynomial, decreasing twice as fast in melt (α_m) as in glass (α_g). There is no evidence of any structural change in either phase. Clay affects α_m slightly and affects α_g considerably. More detailed analysis (see Figure 14.7) of the MMT effect on α_m and $d\alpha_m/dT$ at ambient P reveals the presence of local minima near $w_{\max} = 3.6$ wt%. Similarly, in Figure 14.8, the isobaric plot of α_g versus MMT content indicates a locally nonmonotonic behavior near that concentration. As shown in Table 14.3, the effect increases with P . The results document a greater effect of clay on α_g than on α_m .

14.3.5 Compressibility and Thermal Expansion of PA-6 and Its CPNCs

As displayed in Figures 14.4 to 14.9, κ and α behave differently across the main transition region of the amorphous and semicrystalline polymers, T_g and T_m respectively. While T_g is embedded within the transition region, T_m separates melt from the supercooled liquid with its small quantity of dispersed crystals. Figure 14.9 shows κ and α versus T dependencies for PA-6 and the two PNCs containing 2 and 5 wt% clay. For

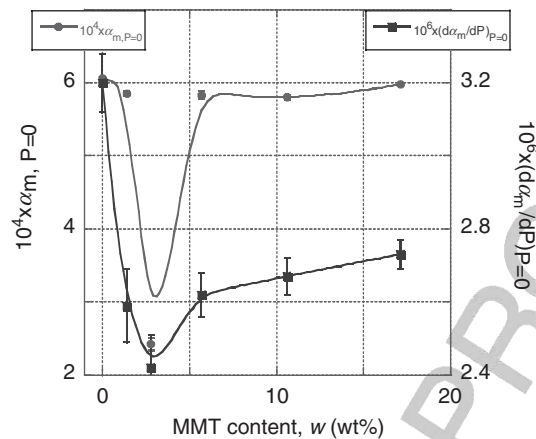


FIGURE 14.7 Concentration dependence of α_m and its first derivative at $P=0$ for PS-based CPNC.

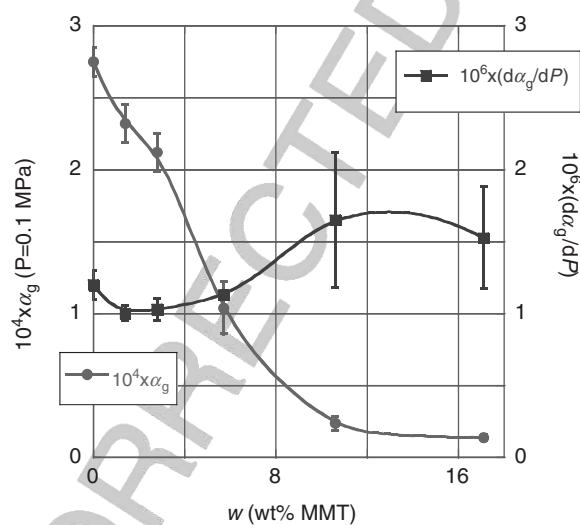


FIGURE 14.8 Concentration dependence of α_g and its pressure derivative at $P=0$ for PS-based CPNC.

TABLE 14.3 Pressure Gradients of the Thermal Expansion Coefficient in the Glassy State, α_g

Sample	$10^4 \times \alpha_0$	$-10^6 \times d\alpha_g/dP$	$10^9 \times d^2\alpha_g/dP^2$	r^2
PS	2.63	1.03	1.73	0.989
PNC-1	2.33	0.97	2.21	0.989
PNC-2	2.16	1.05	2.81	0.997
PNC-5	0.966	1.16	3.83	0.995
PNC-10	0.321	1.49	6.48	0.941
PNC-17	0.213	1.35	5.43	0.917

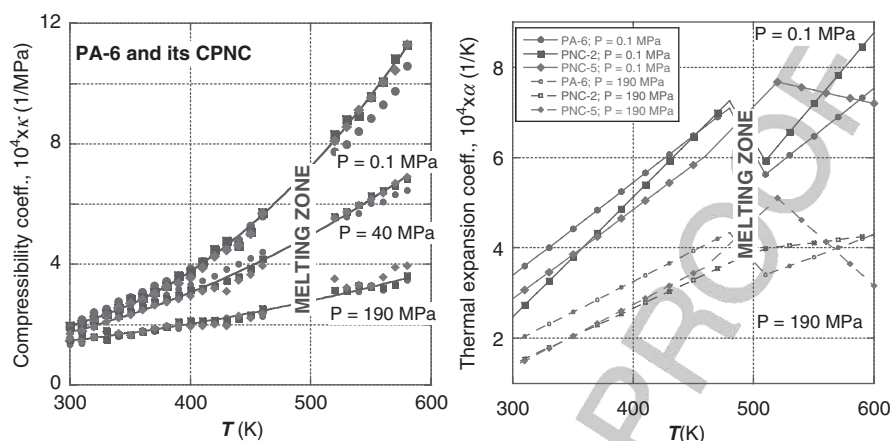


FIGURE 14.9 (a) Compressibility and (b) thermal expansion coefficients for PA-6 and its two PNCs at three and two levels of P , respectively (circles, squares, and diamonds represent data of PA-6, PNC-2, and PNC-5, respectively). (From Utracki [2009b].)

clarity only limited data are shown at three and two pressures, respectively. It is evident that compressibility is a bit affected by clay; it is reduced in solid and increased in the molten state. Characteristically, as predicted by theory, the isobaric values of κ follow nearly the same dependence on both sides of the melting zone [Utracki, 2009].

The situation is quite different for the thermal expansion coefficient, α . Addition of clay slightly reduce its value in the solid state, but it affects it strongly in the melt. Characteristically, melting of PA-6 initially decreases α , while that of PNC-5 increases it—the latter effect most likely is related to the thermal decomposition of clay intercalant.

This terminates the routine analysis of the PVT data, where one obtains the $V = V(T, P)$ and the two derivatives, with the possibility of detecting the secondary transitions, pertinent for polymer processing and performance of the finished products. To extract additional information from these data (i.e., free volume and the interaction parameters), an adequate and realistic theory is required. For this purpose the equations of state need to be employed.

14.4 FREE-VOLUME CONTENT AND INTERACTION PARAMETERS

The main method of the PVT data analyses of amorphous and semicrystalline polymers and their nanocomposites follows a similar sequence:

1. *Melt*. From the melt data, calculate P^* , T^* , V^* and the hole function, $h = h(V, T)$, and analyze the source of observed variability [e.g., effects of molecular weight (M_w), composition (w), degree of dispersion (d_{001}), structure]. Then

extract from P^* , T^* , V^* the L-J binary interaction parameters, ε^* and v^* , valid in the entire range of P and T .

2. *Main transition.* In amorphous systems, determine $T_g = T_g(P, w)$ and the corresponding hole fractions at T_g : $h_g = h_g(P, w)$. In semicrystalline systems, calculate T_m as well as the width and height of the melting region, ΔT_m and ΔV_m , respectively.
3. *Solid body.* In amorphous systems, calculate the hole fraction in the vitreous state, $h = h(P', T')$, and then the pressure and composition dependencies of the frozen free-volume fraction, $FF = FF(P, w)$. The semicrystalline systems must be treated as supercooled liquids (described by the S-S equation of state) comprising dispersed crystals, described by the Midha–Nanda–Simha–Jain equation of state [see Eqs. (6.32) to (6.34)].

14.4.1 Single-Phase Liquids

The reproducibility of the PVT measurements is displayed in Figure 14.1, where results from five independent runs in the full range of P and T nearly superimpose. As in the preceding publications, the experimental data at $T > T_g$ were fitted to the S-S equation of state following a two-step procedure (i.e., calculation of the initial P^* , T^* , V^* parameters from the polynomial approximation of the S-S equation of state [Utracki and Simha, 2001a] and then optimizing the simultaneous fit of data to Eqs. (14.2) and (14.3) [Simha et al., 2001; Utracki et al., 2003; Utracki and Simha, 2004; Utracki, 2007]). Table 14.4 lists the P^* , T^* , V^* parameters, the segmental molecular weight, M_s , and the goodness-of-fit measures for V : σ = standard deviation and r^2 = correlation coefficient squared. Judging by the small values of σ and the large values of r^2 , the S-S equation of state describes the PVT data well. Different values of the characteristic reducing parameters for polymers that are chemically the same should be noted; both the molecular weight and the industrial additives affect these values [Utracki, 2007a]. Poorer results for PPE are due to degradability at high temperature and limited number of data points. In all these calculations, $3c/s = 1 + 3/s \approx 1$ was assumed. The influence of this assumption on the L-J interaction parameters computed has been discussed frequently [Prigogine et al., 1957; Jain and Simha, 1980; Utracki, 2005]; see also Chapter 6.

A linear correlation has been observed between ε^* and v^* : $\varepsilon^* = 13.44 + 0.445v^*$ with $r = 0.95$. Similar tendencies are also valid for the present set of data. Considering the limited number of polymers studied, the average interaction parameters for PS are $\varepsilon^* = 32.7 \pm 0.9$ kJ/mol and $v^* = 48.1 \pm 1.4$ mL/mol, confirming the previous findings. For PC, $\varepsilon^* = 33.2$ and $v^* = 34.9$, and for PPE, $\varepsilon^* = 29.6$ and $v^* = 33.6$, indicating a lower value of v^* , which probably originates in the main-chain flexibility engendered by the presence of an oxygen atom [Flory, 1969].

As discussed in Chapter 6, molecular modeling and neutron scattering experiments greatly improved understanding of the liquid structures and their variability with T . The mode-coupling theory (MCT) originates from analysis of the flow behavior near a critical point involving nonlinear correlation functions [Kawasaki, 1966].

TABLE 14.4 Characteristic Reducing Parameters and the Statistical Fit Data for Polymers and Amorphous Blends

No.	Polymer	P^* (bar)	T^* (K)	$10^4 \times V^*$ (mL/g)	M_s	σ	r^2
1	PS-686	7,139 \pm 41	12,811 \pm 49	9,630 \pm 8	51.64	0.00045	0.9999998
2	PS-667	7,741 \pm 12	11,736 \pm 9	9,516 \pm 2	44.30	0.00068	0.9999995
3	PS-1301	7,435 \pm 26	11,723 \pm 22	9,526 \pm 5	45.87	0.00111	0.9999987
4	PS-Z110	8,044 \pm 46	12,256 \pm 37	9,581 \pm 7	52.08	0.00097	0.9999990
5	PS-Z34	8,277 \pm 34	12,030 \pm 34	9,579 \pm 5	52.07	0.00058	0.9999997
6	PS-Z9	8,407 \pm 33	11,873 \pm 25	9,612 \pm 5	52.06	0.00062	0.9999996
7	PS-Z09	7,759 \pm 28	10,050 \pm 25	9,839 \pm 4	52.06	0.00101	0.9999990
8	PS	6,725 \pm 19	9,923 \pm 8	9,575 \pm 3	42.71	0.00108	0.9999990
9	PMMA	8,588 \pm 23	9,663 \pm 7	8,366 \pm 2	37.28	0.00080	0.9999993
10	PA-6	12,574 \pm 82	11,134 \pm 32	8,919 \pm 10	27.51	0.00112	0.9999990
11	PA-6 (1022B)	10,641 \pm 108	12,287 \pm 61	9,199 \pm 15	34.78	0.00115	0.9999999
12	PC	9,521 \pm 65	11,986 \pm 35	8,167 \pm 8	42.72	0.00089	0.9999990
13	PC	7,776 \pm 20	9,739 \pm 7	8,160 \pm 2	42.33	0.00085	0.9999992
14	PPE-126C	8,796 \pm 106	10,672 \pm 60	8,696 \pm 20	38.67	0.00152	0.9999977
15	PPE/PS	8,323 \pm 59	11,668 \pm 39	9,155 \pm 10	42.44	0.00127	0.9999984
16	LDPE60	6,174 \pm 10	10,479 \pm 7	11,713 \pm 2	40.16	0.00046	0.9999999
17	LDPE65	6,092 \pm 12	10,484 \pm 8	11,716 \pm 2	40.71	0.00059	0.9999998
18	LLDPE	6,220 \pm 10	10,571 \pm 7	11,735 \pm 2	40.13	0.00041	0.9999999
19	HDPE	6,189 \pm 17	9,022 \pm 10	11,893 \pm 5	33.97	0.00091	0.9999995
20	PP	5,480 \pm 13	9,042 \pm 7	11,753 \pm 4	38.90	0.00098	0.9999995
21	PP-6523	6,043 \pm 79	10,535 \pm 56	11,827 \pm 24	40.80	0.00204	0.9999970

The MCT theory describes “an ideal liquid-to-glass transition,” a transition from ergodic dynamics for liquids to nonergodic dynamics for glass through a cross-point, $T_c \approx 1.2T_g$ [Götze, 1999; Götze and Sjögren, 1992, 1995]. The transition is dynamic in nature, derived through the structure factor and dependent on temperature and density. The molecules are visualized as enclosed in cages formed by their neighbors and described by the density autocorrelation function. The cage trapping effect increases with density or with cooling: The pertinence of this approach to the glass transition is evident. For example, the high-frequency compressibility spectra show a liquidlike behavior at $T > T_c$, followed by a dual behavior at T_c and then a “classical” α -process behavior associated with glass [Götze and Sjögren, 1988].

Thus, MCT indicates the presence of two structures with different density or temperature dependence for their relaxations, with a crossover transition at T_c . However, there are two questions: whether the ideal and the experimental (or thermal) T_g 's are related, and if so, how they are related. The answer to the first question is affirmative: Segmental relaxation dominates at $T > T_c$, whereas structural relaxation dominates at $T < T_c$, for low-molecular-weight solvents as well as for molten polymers. The answer to the second question is more complex. The existence of transition temperatures T_g

and T_c has been reported for many fragile glass-forming liquids where their ratio, $T_c/T_g = 1.19$ to 1.68 , depends on the fragility index [see Eq. (14.17)] [Angell, 1985, 1995; Böhmer et al., 1993; Murthy and Kumar, 1993; Rao et al., 2001; Buhot and Garrahan, 2002]. One cannot argue that the difference between T_g and T_c stems from different measuring methods (e.g., involving either a different quenching rate or test frequency). The T_c transition temperature coincides with Boyer's liquid-liquid transition temperature, $T_{LL}/T_g = 1.20 \pm 0.05$ [Boyer, 1977, 1980, 1985, 1987] and with Ngai's T_B crossover temperature [Ngai, 2000, 2003]. In short, for decades, T_g and a transition temperature secondary to it, $T_c \approx T_B \approx T_{LL}$, has been observed on the same function (e.g., viscosity or dielectric relaxation versus T) [Patterson et al., 1976; Murthy, 1990, 1993]. Götze wrote: "It is not possible, however, to identify the critical temperature T_c of the theory for the ideal glass transition with the experimental glass transition temperature, T_g " [Götze and Sjögren, 1988, 1992, 1995; Götze, 1999]. Several other approaches have been explored (i.e., entropic, energy landscape, frustration-based, and others reviewed by Debenedetti and Stillinger [2001], Reichman and Charbonneau [2005], and Tarjus et al. [2005]). The TFT identifies T_c as an onset of fractal aggregate formation and T_g as the temperature at which their concentration reaches the percolation level, ϕ_p and the melt vitrifies [Wool, 2008a,b]. In the case of PS and PS-based CPNC, T_c was nondetectable on the PVT surface but quite evident in $\kappa = \kappa(P, T)$ plots at $T_c \approx 1.2T_g$, while T_g was readily determined from the PVT data and confirmed by DSC.

The transition at T_c is real and pertinent for a number of physical properties. Its effect on viscosity, viscoelasticity, and compressibility has been mentioned. PALS relates the third exponential component of the metastable *ortho*-positronium (*o*-Ps) to the free volume in a polymer. The parameters extracted from the spectrum are the lifetime, τ_3 (related to the average hole size $\langle v_h \rangle$); the intensity, I_3 ; and the volume dispersion, σ_3 . There is a local linear relation between τ_3 or σ_3 and T , local since plots of these parameters versus T display transition points, one at T_g and another one at T_{kv} or $T_{k\sigma}$, respectively. The latter transition temperatures, known as knees, indicate the highest temperature above which the PALS signal, τ_3 or σ_3 , no longer increases. The origin of the knees might be too-fast structural motion, causing the hole walls to move during the *o*-Ps lifetime and thus placing a boundary between the cold (heterogeneous) and warm (homogeneous) liquids [Dlubek et al., 1998, 2007].

Table 14.5 shows a similar trend in T_{kv} to that of T_c . For example, depending on the sample and the parameter used for knee detection, the ratio $T_{kv}/T_g = 1.19$ to 1.68 , and coincidentally, the experimental range of T_c/T_g is the same. These variations might be related to the glass-former fragility index, defined as

$$m_g(\tau) \equiv \left. \frac{d \log \tau}{d(T_g/T)} \right|_{T=T_g} \simeq 250 - 320\beta \quad (14.17)$$

$$T_{kv}/T_g \cong 1.86 - 0.0043m_g; \quad r = 0.77$$

TABLE 14.5 Fragility Index, m_g , and T_k/T_g Ratio for Polymers

No.	Polymer	m_g	T_{kv}/T_g	$T_{k\sigma}/T_g$	Reference
1	PVAc	95	≥ 1.36	—	Wang et al. [1998]
2	PMMA	145	≥ 1.28	—	Wang et al. [1998]
3	1,4-PBD	99 (85)	1.62	—	Bartoš and Krištiak [1998]
4	<i>cis</i> -1,4-PBD	(84)	1.54	—	Bartoš et al. [2000]
5	PIB	46	≥ 1.44	—	Bartoš et al. [2000]
6	PS	139	1.23	—	Dlubek et al. [2003]
7	SAN (0–50%AN)	—	1.22	—	Dlubek et al. [2004]
8	PMMA	145	1.21	≥ 1.25	Kilburn et al. [2006a]
9	Epoxy	151 (94)	1.31	1.23	Dlubek et al. [2006]
10	PIB	46	1.68	1.55	Kilburn et al. [2006b]
11	Perfluoroelastomer	—	1.55	1.36	Dlubek [2006b]
12	PMPS	100	1.19	1.19	Dlubek et al. [2007]

where β is the Kohlrausch exponent in the relaxation function: $\Theta(t) \sim \exp[-(t/\tau)^\beta]$. According to Dlubek [2008], usually, $T_{k\sigma} < T_{kv}$ (see also Table 14.5), so the standard deviation of the lifetime distribution, σ_3 , stops growing while $\langle v_h \rangle$ continues to follow a normal thermal expansion. Thus, the knee in $\langle v_h \rangle$ might be related to the structural motions, while $T_{k\sigma}$ indicates that the subvolume $\langle V_{SV} \rangle \sim 1/\sigma^2$, which contains a single hole, became constant, independent of temperature.

The empirical dependence of T_{kv}/T_g on m_g in Eq. (14.17) has a low correlation coefficient, originating from different sources of values for the two variables and the limited number of data points. Nevertheless, the information collected shows remarkable similarity between T_{kv}/T_g and T_c/T_g . This is discussed in greater detail in Chapter 11.

14.4.2 Polymeric Nanocomposites

Analyses of the *PVT* behavior of several CPNCs have been published. The results are summarized in Table 14.6, with angle brackets indicating average responses (the single-phase systems are listed in Table 14.4). The statistics confirm that the S-S equation of state describes the *PVT* surfaces of CPNCs accurately, with the standard error of the measurement in V (i.e., $\sigma = 0.0005$ to 0.0026 and $r^2 \geq 0.99999$).

Fitting homopolymer *PVT* data to the S-S equation of state provides two sets of information: (1) the free volume content, $h = h(P, T)$ or $h = h(\tilde{P}, \tilde{T})$, and (2) the binary L-J interaction parameters. For PNC the procedure also provides the function $h = h(P, T)$, and the average reducing parameters, $\langle P^* \rangle$, $\langle T^* \rangle$, and $\langle V^* \rangle$. These might be used to calculate the h -value at any temperature and pressure, as required when comparing the *PVT* data with other physical measures (e.g., flow properties [Utracki and Sedlacek, 2007; Chapter 16 in this book] or PALS [Schmidt and Maurer, 2000]. The discussion of free volume in CPNC and on the L-J parameters follows in Sections 14.4.3 and 14.4.4.

TABLE 14.6 Characteristic Reducing Parameters and the Statistical Fit Data for CPNCs

Matrix	Clay (wt%)	$\langle P^* \rangle$ (bar)	$\langle T^* \rangle$ (K)	$10^4 \times \langle V^* \rangle$ (mL/g)	M_s (g/mol)	$\langle \varepsilon^* \rangle$	$\langle v^* \rangle$	σ	r^2	CD	Ref. No. ^a
PA-6	0	12,574 ± 82	11,134 ± 32	8,919.3 ± 9.6	27.51	31.23	24.54	0.00112	0.999999	0.998602	1
PA-6	0.8	11,857 ± 111	11,364 ± 49	8,943.1 ± 14.3	29.70	31.49	26.56	0.00145	0.999998	0.998501	1
PA-6	1.6	11,639 ± 126	11,307 ± 54	8,888.6 ± 16.2	30.29	31.71	26.92	0.00127	0.999998	0.998550	1
PP	0	5,727 ± 68	10,449 ± 57	11,728 ± 22	43.1	28.954	50.565	0.00165	0.999998	0.999275	2
PP-2	1.14	5,169 ± 103	10,712 ± 98	11,874 ± 37	48.4	29.683	57.427	0.00192	0.999998	0.999098	2
PP-3	1.59	5,457 ± 55	10,775 ± 49	11,712 ± 18	46.7	29.860	54.695	0.00184	0.999998	0.998890	2
PP-2-E	1.14	5,230 ± 117	11,251 ± 120	12,060 ± 42	49.4	31.179	59.615	0.00250	0.999996	0.998340	2
PP-2-3	1.13	4,923 ± 99	10,970 ± 101	11,971 ± 37	51.9	30.401	61.752	0.00248	0.999996	0.998549	2
PP-2G	1.23	5,247 ± 95	10,848 ± 90	11,993 ± 34	47.8	30.063	57.295	0.00226	0.999997	0.998731	2
PP-4	2.42	5,028 ± 93	10,917 ± 92	11,857 ± 34	50.7	30.251	60.172	0.00227	0.999997	0.998749	2
PP-E	0	5,111 ± 95	10,820 ± 91	11,926 ± 34	49.2	28.958	50.565	0.00235	0.999997	0.998707	2
PP-4-E	2.19	5,826 ± 117	10,647 ± 96	11,662 ± 37	43.4	30.097	53.506	0.00258	0.999996	0.998145	2
PP-4-3	2.28	5,266 ± 93	10,993 ± 91	11,931 ± 33	48.5	30.465	57.853	0.00255	0.999996	0.998231	2
PP-4G	2.12	5,203 ± 96	10,952 ± 94	11,807 ± 34	49.4	30.353	58.341	0.00227	0.999997	0.998682	2
PS	0	7,435 ± 26	11,723 ± 22	9,525.9 ± 4.7	45.869	31.983	43.035	0.00111	0.999999	0.999442	3
PNC-1	1.4	7,492 ± 52	11,938 ± 46	9,583.7 ± 9.6	46.079	33.075	44.017	0.00142	0.999998	0.999061	3
PNC-2	2.8	7,475 ± 32	12,010 ± 29	9,567.8 ± 5.9	46.537	33.291	44.534	0.00093	0.999999	0.999587	3
PNC-5	5.7	7,556 ± 56	11,975 ± 48	9,458.8 ± 9.8	46.433	33.291	44.260	0.00150	0.999998	0.998940	3
PNC-10	10.6	7,471 ± 84	11,834 ± 74	9,259.6 ± 15.1	47.407	32.828	43.952	0.00239	0.999994	0.997189	3
PNC-17	17.1	7,510 ± 89	11,711 ± 73	9,011.2 ± 14.6	47.770	32.476	43.290	0.00259	0.999992	0.996789	3
PA-6	0	12,328 ± 60	11,157 ± 22	8,935.5 ± 6.9	28.069	30.916	25.081	0.00133	0.999998	0.998530	4
PA-C2	1.6	13,104 ± 69	10,962 ± 22	8,779.3 ± 7.4	26.408	30.977	23.184	0.00145	0.999998	0.998217	4
PA-C5	4.0	13,120 ± 86	10,956 ± 28	8,685.2 ± 9.2	26.642	30.359	23.139	0.00172	0.999997	0.997433	4
PA-6	0	10,641 ± 108	12,287 ± 61	9,199 ± 15	34.78	34.05	32.00	0.00115	0.999999	0.998615	5
PNC-2	2.29	11,808 ± 122	11,338 ± 52	8,895 ± 15	29.82	31.42	26.52	0.00143	0.999998	0.998303	5
PNC-5	4.91	12,173 ± 143	11,204 ± 57	8,795 ± 17	29.00	31.05	25.51	0.00153	0.999998	0.998128	5

^a 1, Utracki et al. [2004]; 2, Utracki and Simha [2004]; 3, Tanoue et al. [2004a, b]; 4, melt compounded, unpublished; 5, Utracki [2009b].

14.4.3 Free Volume in PNCs

Figure 6.4 displays the ratios $V(\text{PA})/V(\text{PNC})$ and $h(\text{PA})/h(\text{PNC})$ at $T = 500$ to 600 K and $P = 0.1$ to 190 MPa determined by fitting the PVT data to Eqs. (14.2) and (14.3). Thus, incorporation of 0.64 vol% of organoclay reduced the matrix specific volume by about 0.8% , as expected from the volume additivity principle. By contrast, the simultaneous reduction of h by 15% was not anticipated. Figure 6.5 shows that at constant organoclay loading, $w = 2$ wt%, the loss of free volume increases linearly with the interlayer spacing, d_{001} [Utracki and Simha, 2004]. As discussed later, the explanation for the loss of free volume is based on solidification of the organic phase on a high-energy clay surface. Of the three polymers shown in Figure 6.5, the commercial CPNC based on PA-6 is fully exfoliated; hence, here 100% of the clay surface is accessible and since the PA–clay interactions are favorable [Tanaka and Goettler, 2002], one may expect a thick solid layer. By contrast, the PNC based on PS is poorly dispersed, with low interlayer thickness and a high percentage of clay-forming stacks, where at best, a single PS macromolecular layer might be present between intercalated clay platelets adsorbed on the stacks' surface. The performance of PP-based CPNC is intermediate, as here the interlayer spacing is larger and thus is capable of accommodating more macromolecules, and TEM shows many exfoliated clay platelets [Utracki et al., 2006]. However, there is no fundamental reason why the clay surface available for solidification, A_{total} , should vary linearly with d_{001} .

It is instructive to speculate how A_{total} would change with clay content, w . Starting at infinite dilution and assuming full exfoliation, initially, A_{total} must increase linearly with w . However, at relatively low clay volume fraction, ϕ_{max} , the free platelet rotation (required for full exfoliation) stops and the platelets begin to form local stacks with progressively decreasing interlayer spacing. It can be shown that $d_{001} \approx 0.99/\phi$, so the full clay surface area availability is limited to $\phi < 0.015$. Accordingly, A_{total} , and its associated loss of free volume, Δh , are expected to go through a maximum. Indeed, this is observed for PS-based CPNCs (e.g., see Figure 14.10) as well as for PA-6-based CPNCs; therefore, the local maxima in Δh occur in intercalated as well as in exfoliated systems. Furthermore, while at low concentration the magnitude of Δh depends on the system (i.e., on the degree of clay dispersion, as in the PS and PA systems shown in Figure 6.5), the concentration for the maximum reduction of free volume was found to be about the same, $w_{\text{max}} \approx 3.6 \pm 0.1$ wt% MMT.

In CPNCs there are several clay concentrations that are expected to cause changes in system performance. Assuming monodispersed, fully exfoliated clay platelets with the aspect ratio $p = d/t = 200$ and the density $\rho = 2.5$ g/mL dispersed in a matrix with $\rho = 1$ g/mL, one finds that the critical volume fraction for free rotation is $\phi_{\text{rot}} = 0.93/p$, increasing to $0.99/p$, or about 0.5 vol%, upon adsorption of a solidified 6 -nm-thick layer. At this concentration the free matrix with bulk mobility disappears and the average thickness of the organic layer around a clay platelet is about 100 nm. Nothing dramatic is to be expected at this concentration, as this is the limit for all platelets to rotate freely. The next step is the formation of structural zones with locally aligned platelets (i.e., stacks), where the interlayer thickness decreases with clay loading. Full solidification with $d_{001} \approx 13$ nm is expected at $\phi_{\text{full}} \approx 0.08$. Thus, the critical

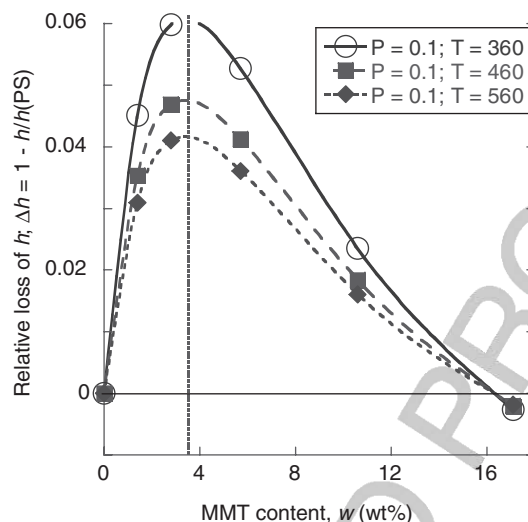


FIGURE 14.10 Relative loss of free volume for the PS-based CPNC at ambient pressure, $P = 0.1$ MPa, and at three temperatures, T (K).

clay concentration observed for the maximum accessible clay surface, $\phi_{\max} \approx 0.015$, corresponds to a layer of low-molecular-mobility organic phase about 30 nm thick on the clay surface.

14.4.4 Lennard–Jones Binary Interaction Parameters

The analyses of PVT data [e.g., calculation of α , κ , $\langle P^* \rangle$, $\langle V^* \rangle$, $\langle T^* \rangle$, and $h = h(P, T)$], have been the same for CPNCs as for single-phase systems. However, whereas for the latter the analysis results in the material-characteristic reducing and interaction parameters, for the former only average values are obtained, and the binary interaction parameters ϵ_{ij}^* and v_{ij}^* are crucial for an understanding of CPNC behavior.

The method used to extract binary interaction parameters from dilatometric data resembles that developed by Simha and his colleagues for filled polymers, summarized in Section 6.4.4. Thus, the clay platelets are treated as giant, rigid molecules. Both components, the matrix and the platelets, are placed on the lattice. The hard-core segmental volumes of both components are assumed to be about equal: $v_{11}^* \cong v_{22}^*$. For the high-molecular-weight matrix polymer, the external degrees of freedom, $3c$, was assumed proportional to the number of statistical segments, s ; hence, $3c_1/s_1 \rightarrow 1$, whereas for clay platelets $3c_2/s_2 \rightarrow 0$ [Simha et al., 2001; Utracki et al., 2003]. As in any multicomponent system, the PVT behavior of PNC is volume-averaged, leading to $\langle P^* \rangle$, $\langle V^* \rangle$, $\langle T^* \rangle$, $\langle \epsilon^* \rangle$, and $\langle v^* \rangle$ parameters. It is noteworthy that in Figure 14.11 the L-J parameters show a similar variation with clay content as does Δh in Figure 14.10, confirming direct links between the free-volume quantity, h , and the L-J interactions.

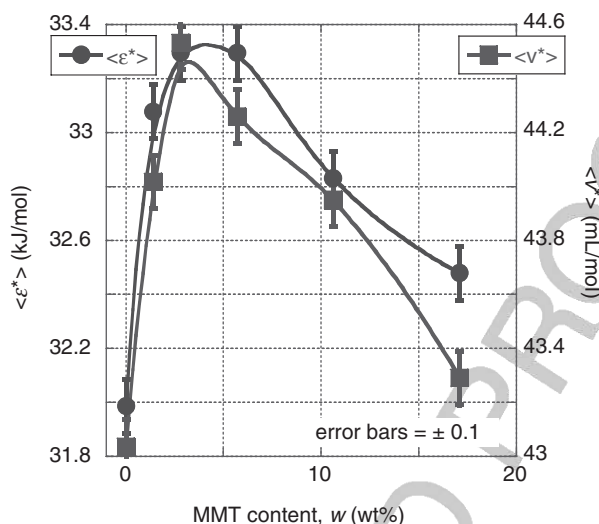


FIGURE 14.11 Concentration dependence of the volume-average L-J interaction parameters for PS and its CPNC.

Utracki [2005] has shown that for polymers, ϵ^* increases with increasing v^*P^* , but since for polymers with a similar chemical structure P^* is similar, a linear relationship between the two L-J parameters is expected; a long time ago, Hirschfelder et al. [1954] reported a linear dependence for gases. For PS of different M_w and polydispersity, $\epsilon^* = 13.4 + 0.445v^*$ ($r = 0.952$) was found. Interestingly, both ϵ^* and v^* increased linearly with $\log M_w$. Although the bulk-averaged parameters for PS-based CPNC in Table 14.6 follow a different least-squares dependence, $\langle \epsilon^* \rangle = -5.23 + 0.868\langle v^* \rangle$, $r = 0.968$, the numerical values of the ϵ^* versus v^* for PS, and $\langle \epsilon^* \rangle$ versus $\langle v^* \rangle$ for CPNC fall within a similar range. Functionally, ϵ^* and v^* define the minimum of the L-J potential; that is, as the strength of interactions increases, the minimum of the L-J potential occurs at increasing distance between the interacting segments—the volume excluded gets larger. However, in the presence of clay, the relation between ϵ^* and v^* is stronger, with the slope nearly twice as large as that for neat PS. To determine the origin of this change it is necessary to extract the individual contribution of the two components: PS and MMT stacks. For this purpose, Eqs. (14.5) to (14.7) will be used with subscripts 1 and 2 assigned to the matrix and solid particles, respectively.

The magnitude of the individual binary interaction parameters, ϵ_{ij}^* , v_{ij}^* , $i, j = 1, 2$, must be computed from the two relations in Eq. (14.5) with six parameters, of which only two (for the matrix, ϵ_{11}^* and v_{11}^*) might be determined directly. The procedure developed for computation of the binary parameters in fully exfoliated PA-6-based CPNCs and in intercalated CPNCs based on PP and maleated polypropylene (PP-MA) have been published [Simha et al., 2001; Utracki et al., 2003; Utracki and Simha, 2004], but application of this strategy to a PS-based system needs to be examined. In the latter system, clay is poorly dispersed in PS, and because of

a wide range of clay content, $w = 0$ to 17.1 wt% MMT, the degree of dispersion decreases due to crowding. Equation (14.5) implies that in binary systems all ε_{ij}^* and v_{ij}^* parameters are independent of concentration. However, owing to the multicomponent nature of CPNCs and concentration-dependent effects of solidification of the organic phase, variability has been observed in the interaction parameters. As mentioned in Section 14.2.1, calculation of the L-J binary interaction parameters for specific CPNCs involves the assumption of a specific structure that might require modification of the two-component model proposed by Jain and Simha [1980, 1984]. There is a multitude of PNC types as well as structures, which may require different models.

The model adopted, hairy clay platelets (HCPs), was formulated considering the reduction of molecular mobility near the clay platelet crystalline surface [Utracki and Lyngaae-Jørgensen, 2002]. The data show that polymer adsorbed from solution or melt on a crystalline solid forms a layer whose thickness is comparable to the radius of gyration, $(s_{\theta}^2)^{1/2}$; the macromolecules adsorb physically on a solid surface, forming structures known as trains, loops, and tails of diverse size. Only at a distance $z_2 = 100$ to 120 nm is the chain mobility the same as in the absence of clay platelets. Consequently, a multicomponent CPNC is treated as a binary system composed of (1) clay platelets or stacks with a solidified $z_1 \approx 4$ - to 6-nm-thick layer of intercalant, compatibilizer, and/or polymer (subscript $i = 1$), and (2) a matrix layer stretching from z_1 onward (i.e., including the second layer of organic phase with reduced molecular mobility). Within the distance from z_1 to z_2 the interaction parameters follow Eq. (14.7). The magnitude of its n -parameter affects the predicted rate of change in the z -direction of the interaction parameters, $\varepsilon_{11}^*(z)$ and $v_{11}^*(z)$, but not the limiting values; a reasonable prediction was obtained assuming that $n = 2$. For the PP-based CPNC the computer program optimized the fit to Eq. (14.7) of the bulk average parameters $\langle \varepsilon^* \rangle$ and $\langle v^* \rangle$, yielding the interaction parameters ε_{22}^* and v_{22}^* , and then the variable matrix interaction parameters $\varepsilon_{ii}^* = \varepsilon_{ii}^*(X_1)$ and $v_{ii}^* = v_{ii}^*(X_1)$ (see Figure 14.12). The variation of the latter parameters is consistent with the linear correlation often observed between them [Utracki and Simha, 2004].

The HCP model implies that in diluted systems ($\phi < 0.005$, where exfoliated clay platelets may freely rotate), individual HCPs are dispersed in a polymeric matrix and values of the interaction parameters are constant. As the concentration increases, the domains of reduced mobility around HCPs begin to overlap, macromolecules with bulk properties disappear, and the interactions change with clay content. Above the encompassed clay platelet volume fraction, $\phi_{\text{rot}} = 0.99/p \approx 0.005$, there is a second critical concentration, $w_{\text{max}} \approx 3.6$ wt% or $\phi_{\text{max}} \approx 0.015$, at which the clay platelets with adsorbed solidified organic phase begin to overlap. Due to platelet crowding, CPNC approaching this concentration forms stacks; thus, the assumption that individual exfoliated platelets are present is no longer valid.

Before the individual L-J parameters are computed from Eq. (14.5), the molar and site fractions (x_i and X_i , respectively) must be calculated [Utracki et al., 2003]:

$$x_1 = \frac{(m_1/M_{s1}) - (m_{1,\text{solid}}/M_{s1})}{(m_1/M_{s1}) + (m_2/M_{s2})} \quad x_2 = 1 - x_1 \quad (14.18)$$

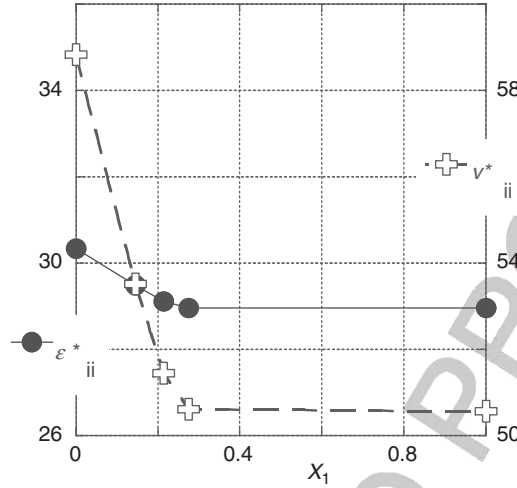


FIGURE 14.12 Changes of the matrix interaction parameters versus the site fraction, X_1 . (From Utracki and Simha [2004].)

where m_1 is the weight fraction of the polymer, $m_{1,\text{solid}}$ is the weight fraction of solidified matrix, m_2 is the weight fraction of clay, and $M_{si} = M_i/s_i$ is the molecular weight of a statistical segment of component i (M_i and s_{iB} are the molecular weight and number of statistical segments, respectively).

The average segmental molecular weight of PS in Tables 14.4 and 14.6 is $M_{s1} = 48.1 \pm 0.9$ g/mol, whereas the molecular weight of styrene is $M_0 = 104.14$ g/mol; thus, one lattice cell accommodates about one-half styrene mer with a hard-core molecular volume of $v_{\text{hard}}^* = M_s V^*/2^{1/2} = 32.38$ mL/mol, or one hard-core statistical segment of clay of a similar volume. The latter rule provides the means for computing the molecular weight of the clay statistical segment, M_{s2} . The clay platelets are assumed to be circular with an average diameter of $d = 200$ nm, thickness $h = 0.96$ nm, and density $\rho = 2.3$ g/mL. Thus, the molecular mass of an average platelet is $M_2 = N_A \rho \pi d^2 h / 4 = 41,772$ kg/mol, and its molecular volume is $V_{\text{plat}} = M/\rho = 4.54 \times 10^6$ mL/mol. In consequence, the number of segments in PS (s_1) and clay (s_2) are, respectively, $s_1 = 2921$ and $s_2 = V_{\text{plat}}/v_{\text{hard}}^* = 3.43 \times 10^5$. Finally, the mass of solidified PS on the surface of a clay platelet can be calculated from the mass of clay and relative volume of clay to solidified polymer. Assuming that the clay surface area is A and that the thickness of the solidified layer is 4 nm leads to $m_{1,\text{solid}} = m_2(8A\rho_1)/(0.96A\rho_2) = 3.805m_2$. These calculations assume that at $\phi < \phi_{\text{max}} = 0.99/p$, clay dispersion is dominated by individual freely rotating clay platelets; hence, within this concentration range the procedure developed for PA-6- or PP-based CPNCs might be used [Utracki et al., 2003; Utracki and Simha, 2004].

At a higher clay content, $\phi > \phi_{\text{max}}$, melt compounding of the PS/C10A system results in progressive (with concentration and residence time) reduction of the inter-layer spacing [Tanoue et al., 2004a,b, 2005]. The XRD data identified two generations of stacks, labeled numbers 1 and 2 for peak 1 and peak 2 at $d_{001} \approx 4.37$ and 1.66 nm,

respectively. High-resolution transmission electron microscopy (HRTEM) showed that the CPNC morphology was dominated by tightly packed stacks corresponding to peak 2 with about six platelets in each. Furthermore, the dimensions and spacing of the stacks were independent of concentration, behaving like effective particles composed of intercalated clay platelets. From the stack geometry the amount of intercalant in a stack was about 24 wt%, whereas neat C10A contains 39 wt%. This indicates that during melt compounding of C10A in PS, in addition to dissolution of excess intercalant (above the clay cation-exchange capacity) in molten PS, Hofmann [1851] elimination takes place.

These arguments suggest that for $\phi \geq \phi_{\max}$ it is appropriate to consider that CPNCs are composed of PS matrix with dispersed stacks of effective diameter ≥ 200 nm and thickness $h_{\text{eff}} \approx 11.4$ nm. Because of the platelets' lateral displacement, the effective diameter of the stack might be significantly larger than 200 nm; thus, their aspect ratio $p_{\text{eff}} \geq 18$, and in consequence the maximum is expected at MMT loadings ranging from $w_{\max} \approx 1.4$ wt% for the fully exfoliated CPNC to $w_{\max} \leq 10.7$ wt% for the intercalated stacks with $p_{\text{eff}} \geq 18$. Because of the tight packing within the stacks, the PS solidification is realistic only on the stacks' surface. The area available for solidification ranges is

$$A = \begin{cases} \frac{w}{h\rho} & \text{at } \phi < \phi_{\max} \\ \frac{w}{h\rho m} & \text{at } \phi > \phi_{\max} \end{cases} \quad (14.19)$$

where w is MMT content in wt% and m is the number of clay platelets per stack. Using Eq. (14.19), one finds that at relatively low MMT content, PS matrix is adsorbed and solidified; thus, further addition of organoclay only dilutes the system. An assumption that the thickness of solidified PS ranges from 6 to 4 nm yielded the limiting concentration for nonsolidified PS: $w_{\max} = 2.5$ to 3.6 wt%, respectively; thus, considering the experimental value of $w_{\max} \approx 3.6$ wt%, the thickness of solidified PS on organoclay is about 4 nm.

The relative loss of the matrix free-volume quantity, h , at ambient P and three temperatures was computed from Eqs. (14.2) and (14.3). The results are displayed in Figure 14.10. The vertical dashed line is for w_{\max} . Thus, the disappearance of the "free" PS at w_{\max} provides an explanation for the presence of local extrema in Figures 14.8, 14.10, 14.11, and 14.15. It is noteworthy that $\Delta h \approx 0$ at 16 wt% MMT, indicating that at $P = 0.1$ MPa and $T = 360$ to 560 K C10A has a higher free-volume content than that of neat PS; this is to be expected considering the amount and type of intercalant present.

Using Eqs. (14.5) to (14.7) the L-J parameters were computed for a two-component system. As before, the cross-interaction parameters, ε_{12}^* and v_{12}^* , were assumed to be given by Berthelot's rule and the algebraic average, respectively [Utracki and Simha, 2004]:

$$\varepsilon_{12}^* = \sqrt{\varepsilon_{11}^* \varepsilon_{22}^*} \quad \text{and} \quad v_{12}^* = \frac{(v_{11}^{*1/3} + v_{22}^{*1/3})^3}{8} \quad (14.20)$$

TABLE 14.7 Binary Interaction Parameters for a PS/MMT Stack System at $\phi > \phi_{\max}$

Parameter $ij =$	Binary Interaction		
	11	12	22
ε_{ij}^*	32.0 ± 0.6	32.5 ± 0.4	33.0 ± 0.1
v_{ij}^*	43.0 ± 1.7	43.6 ± 0.9	44.2 ± 0.1

For ease of computation, Eq. (14.5) was transformed into [Utracki, 2004]

$$\begin{aligned}
 \langle v^* \rangle^2 &= \frac{\varepsilon_4}{\varepsilon_2} \times v_{11}^{*2}; \quad \text{and} \quad \langle \varepsilon^* \rangle = \frac{\varepsilon_2^2}{\varepsilon_4} \times \varepsilon_{11}^* \\
 \varepsilon_2 &\equiv X_1^2 + 2X_1X_2e_{12}v_{12}^2 + X_2^2e_{22}v_{22}^2 = \left(\frac{\langle v^* \rangle}{v_{11}^*} \right)^2 \left(\frac{\langle \varepsilon^* \rangle}{\varepsilon_{11}^*} \right) \\
 \varepsilon_4 &\equiv X_1^2 + 2X_1X_2e_{12}v_{12}^4 + X_2^2e_{22}v_{22}^4 = \left(\frac{\langle v^* \rangle}{v_{11}^*} \right)^4 \left(\frac{\langle \varepsilon^* \rangle}{\varepsilon_{11}^*} \right)
 \end{aligned} \quad (14.21)$$

where $e_{12} \equiv \varepsilon_{12}^*/\varepsilon_{11}^*$, $e_{22} \equiv \varepsilon_{22}^*/\varepsilon_{11}^*$, $v_{12} \equiv v_{12}^*/v_{11}^*$, and $v_{22} \equiv v_{22}^*/v_{11}^*$.

Equations (14.20) and (14.21) were solved using the Scientist nonlinear least-squares protocol from MicroMath. The computed ε_{ij}^* and v_{ij}^* are listed in Table 14.7. Since the calculations were made for stacks with externally solidified matrix, only the $\phi > \phi_{\max}$ data were used. The least-squares fit yielded $r^2 = 0.99997$. The ratio obtained, $v_{22}^*/v_{11}^* = 1.03$, is well within the theoretically acceptable range for the cell-size variation [Papazoglou et al., 1989]. As noted before, here also both interaction parameters increase from values measured for PS to those computed for the organoclay stacks. The increase is small, but as was the case for the bulk-averaged parameters, it is larger for ε_{22}^* than for v_{22}^* ; thus, even the stacks covered by intercalant and solidified PS interact more strongly between themselves than PS segments do.

14.4.5 Structure and Transitions Within the Molten Phase

As discussed in Section 14.4.1, molecular modeling and dynamic scattering experiments have been used for studies of liquid structures at $T > T_g$ [Jäcke, 1986; Kanaya and Kaji, 2001; Binder et al., 2003; Bicerano, 2003; Paul, 2004]. While cooling from a high-temperature melt, the liquid is subjected to several changes in its structure. There is a dynamic crossover at $T > T_g$, interpreted in terms of different mechanisms. MCT considers that in liquids there are two relaxations: segmental (at $T > T_c$) and structural (at $T < T_c$). For polymers, the crossover transition temperature takes place at $T_c/T_g \approx 1.25 \pm 0.10$ [Kisliuk et al., 2000]: that is, within the range of the controversial Boyer's liquid-liquid transition temperature, $T_{LL}/T_g = 1.2 \pm 0.1$ [Boyer, 1977, 1980, 1985, 1987]. There are also other relaxation processes, such as the fast and the elementary. The former starts near the Vogel-Fulcher-Tammann-Hesse (VFTH) temperature in the glassy state and stretches to $T > T_c$, whereas the latter is related to conformational transitions that extend to temperatures well above T_c [Ngai, 2000, 2003]. TFT considers T_c to be the starting temperature for twinkling aggregate formation, which at T_g reaches the percolation threshold, ϕ_p [Wool, 2008a,b; Wool and Campanella, 2009].

Since the T_{LL} , T_c , T_B , or unprejudiced T_T transition is weak, it is seldom visible on the PVT surface, but is evident in derivatives [e.g., in plots of $\kappa = \kappa(P, T)$ versus T]. This dependence is shown in Figure 14.4 for three samples: PS, PNC-2, and PNC-17. Several phenomena are worth noting: (1) the transitions $T_g(0)$ and T_T are virtually pressure independent; (2) owing to the plasticization by intercalant, T_{g1} decreases with organoclay loading; (3) the transition region stretches from $T_g(0)$ to T_T ; (4) for the three systems, $T_T/T_g = 1.17, 1.19$, and 1.19 ± 0.01 , respectively (only at $T > T_T$ does κ increase linearly with increasing T); (5) in vitreous PNC-17 at low pressures κ increases with increasing T but decreases at high P ; (6) the clay effects are evident in the molten state, especially at high pressures (at $P = 190$ MPa and $T > T_T$ the coefficient κ increases with increasing T for PS, is constant for PNC-2, and decreases for PNC-17); (7) the relative compressibility, $\kappa_R \equiv \kappa(\text{PNC} - 17)/\kappa(\text{PS})$, changes at $300 \leq T(\text{K}) \leq 430$ (i.e., within the transient region, **T**); and (8) within the $T < T_T$ range, κ_R suggests that different mechanisms are responsible for the PVT behavior of CPNCs than for that of PS.

Figure 14.5 shows the κ -behavior of PS-based CPNCs, similar to that observed for PS-686 studied by Quach and Simha or PS-Z110 measured by Zoller following a standard procedure. Quach and Simha measured the PVT surface isobarically by cooling from $T \approx T_g + 30$ to ambient temperature, then remelting it at this temperature, increasing the pressure, and cooling at a rate of $10^\circ\text{C}/\text{min}$ to the next level of temperature. Both these data sets show a secondary transition at $T_T/T_g \approx 1.22$ or 1.23 , close to the crossover transition temperature, $T_c/T_g \approx T_{LL}/T_g = 1.25 \pm 0.10$. All these transitions fall within the same relative temperature range: $T \approx T_T$. It is noteworthy that for six decades or so the amorphous polymers have been processed at $T \geq 60 + T_g$; hence within the structureless range of melts at $T > T_T$ where, as we know today, polymer melt is homogeneous.

14.5 FREE VOLUME IN THE GLASSY STATE

14.5.1 Glass Transition Temperature Region

As shown in Figures 14.1, two graphical procedures were employed for determining T_g from PVT diagrams; the first defines T_{g1} by the limit of the linear decrease of the abscissa upon cooling of V versus T or $\ln V$ versus $T^{3/2}$, while the other, T_{g2} , adopts the intersection of slopes of these dependencies in the molten and glassy states. At ambient pressure both methods yield similar results, but as the pressure increases and a large transitory zone **T** appears between the glassy and molten regions, the differences become progressively large, $\Delta T_g = |T_{g1} - T_{g2}| \leq 50^\circ\text{C}$. The problem becomes more acute for CPNCs since in the glassy state the specific volume may decrease upon heating rather than flattening out, and start increasing near T_g .

The dependence $T_g = T_{g1}(P)$ was determined from the isobaric $\ln V$ versus $T^{3/2}$. The values of T_g were taken at the boundary between the molten and transition zones. The dependence, $T_g = T_{g1}(P, w)$, for PS and its CPNC in Figure 14.13 follows the second-order polynomial; its a_i parameters are listed in Table 14.8. The concentration dependence of $a_0 = T_{g, P=0}$ is displayed in Figure 14.3 along with the ambient

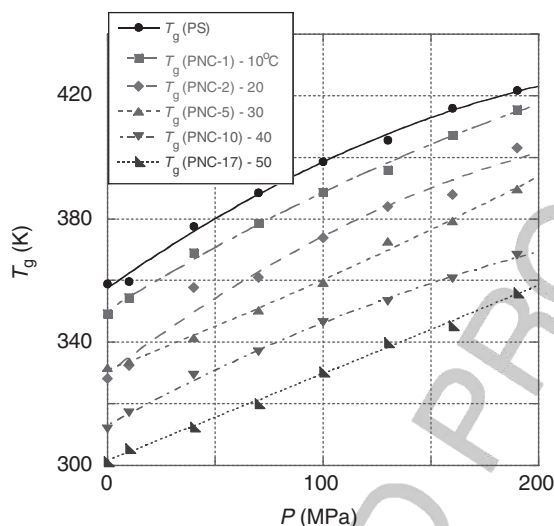


FIGURE 14.13 Pressure dependence of $T_{g1} = T_g$ for PS and its CPNC. For clarity the constant composition data are displaced vertically from each other by 10°C each.

pressure T_g determined by DSC at two scan rates, 2 and $20^\circ\text{C}/\text{min}$, and then extrapolated to zero scan rate. The two sets of data are in reasonable agreement. The other parameters, a_1 and a_2 , depend on composition: $a_1 = 0.480 - 0.0118w$ with $r = 0.79$, and $a_2 \times 10^4 = -7.31 + 0.406w$ with $r = 0.77$, from which the derivatives $dT_g(P)/dP$ and $d^2T_g(P)/dP^2$ might be calculated. At ambient pressure the first derivative decreases with increasing clay loading from $a_1 = dT_g/dP|_{P=0} = 0.480$ to 0.278 (K/MPa), while the second derivative increases from -1.46×10^{-3} to -7.35×10^{-5} .

Figures 14.13 to 14.15 demonstrate that T_g increases with increasing P and decreases with increasing w , while the free-volume quantity, $h_g = h_g(T_g, P_g)$, decreases with both P and w . Its value at ambient pressure and that of the pressure gradient, dh_g/dP , are listed in Table 14.8 and displayed in Figure 14.15 as functions of the MMT content. Numerical values of the polynomial fitting to h_g are also listed in

TABLE 14.8 Pressure Dependence of the Glass Transition Temperature $T_{g1} = \sum a_i P^i$, and the Hole Fraction at T_g : $h_g = h_{g0} + b_1 P$ (MPa)

Sample	$T_{g1,P=0}$ (PVT)	a_1	$a_2 \times 10^4$	r	$T_{g,P=0}$ (DSC)	h_{g0}	$-b_1 \times 10^4$	r
PS	357.6	0.491	-8.14	0.998	365.4	0.0682	7.40	0.991
PNC-1	360.4	0.430	-4.78	0.998	364.9	0.0650	7.16	0.994
PNC-2	349.9	0.531	-8.65	0.989	363.4	0.0608	5.36	0.915
PNC-5	361.0	0.271	-2.12	0.998	362.0	0.0639	8.00	0.969
PNC-10	353.0	0.383	-5.11	0.999	360.9	0.0637	8.44	0.997
PNC-17	351.6	0.280	0.232	0.998	357.1	0.0638	8.60	0.981

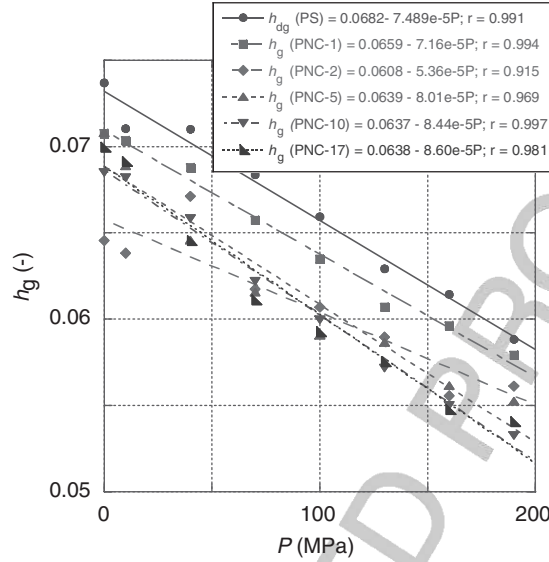


FIGURE 14.14 Pressure dependence of the free-volume parameter h at T_g for PS and its CPNC.

Table 14.8. The pressure gradients of T_{g1} and h_g show local extrema at $w_{\max} = 3.6$ wt%. For neat polymers a reciprocal dependence on P was observed for T_g and h_g [Utracki, 2007a], but for highly loaded CPNC such a relationship is more complicated, especially near the MMT concentration where the free PS disappears, $w_{\max} \approx 3.6$ wt%. It is expected that with increasing pressure, T_g should increase and h_g should decrease.

The temperature dependence of h changes across T_g . In the melt the macromolecules are at the thermodynamic equilibrium and the free volume depends on P and T . In the glassy state h also depends on the way the glass was prepared, including the aging time, t_a [i.e., $h = h(P, T, t_a)$]. At T_g a part of the free volume becomes frozen, causing $h = h(T)_{P=\text{const}}$ to become a less sensitive function of temperature below T_g than above. In contrast to T_g and its derivatives in Figures 14.3, 14.13, and 14.16, the h_g nonlinearly varies with clay content. The data in Figure 14.15 suggest that CPNC with about $w_{\max} = 3.6$ wt% MMT is most sensitive to P . For the phase equilibrium such a high sensitivity would indicate binodal conditions (note that C10A is immiscible with PS).

In an earlier paper it was found that the theoretical prediction of Eq. (14.9) is correct only in systems vitrified by isobaric cooling from the melt [Utracki, 2007a, Fig. 12]. By contrast, for polymers tested using the standard *PVT* procedure, the values of dT_g/dP calculated increased with pressure while the experimental gradient was about constant. Judging by the dependencies in Figure 14.16, for CPNC the gradient depends on P and w . Thus, addition of a small amount of organoclay, as in PNC-1, increased the gradient dT_g/dP above that of PS and caused a more rapid

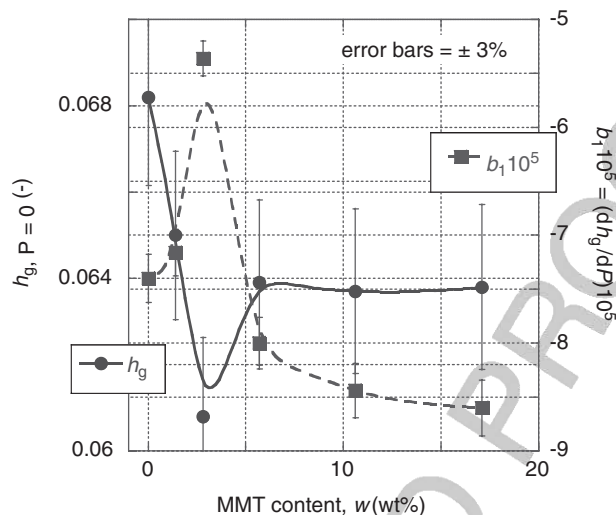


FIGURE 14.15 Composition dependence of h_g and its P -gradient for PS and its CPNC at ambient P .

decrease with pressure. By contrast, addition of larger amounts, as in PNC-17, reduced the ambient pressure value of dT_g/dP and made it a slightly increasing function of pressure. For systems containing 1.4 to 17.1 wt% MMT, the gradient decreases with increasing pressure toward zero. Incorporation of organoclay into a system devoid of free matrix (i.e., at $w > 3.6$ wt%) increases dT_g/dP slightly. It is noteworthy that

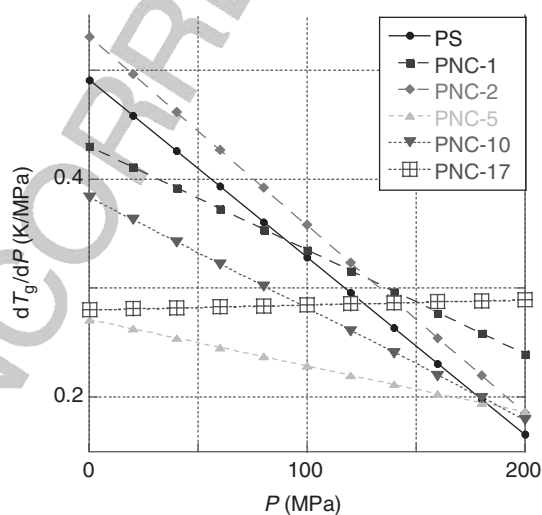


FIGURE 14.16 Pressure gradient of T_g for PS and its CPNC as a function of P .

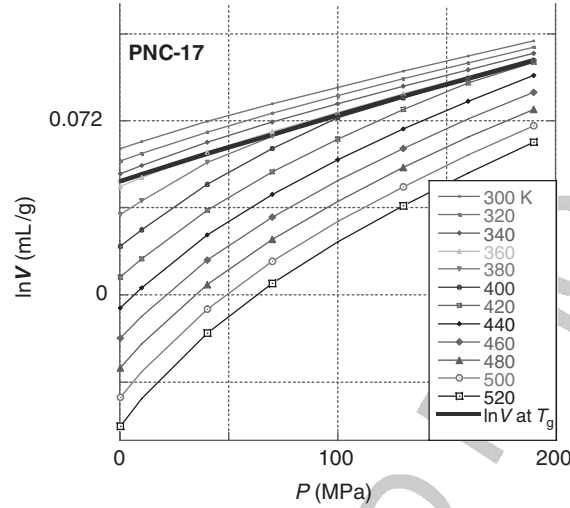


FIGURE 14.17 Isothermal specific volume of PNC-17 versus P . See the text.

for PS the $a_1 = (dT_g/dP)_{P=0}$ ranges from 0.16 to 0.31 K/MPa [Roe, 1987]. In more recent studies the gradient for amorphous polymers was $a_1 = 0.29$ to 0.78 [Utracki, 2007a]; thus, the values listed in Table 14.8, $a_1 = 0.28$ to 0.49, fall within these wider limits.

The generalized Ehrenfest equation, Eq. (14.10), assumes that vitrification is a second-order pseudoequilibrium process—neither the rate nor the vitrification method (e.g., cooling versus compression) is taken into account. Furthermore, there is a basic problem in calculating the individual contributions. For example, in the isobaric plots in Figure 14.13, T_g increases with increasing P by about 60 K, but the isothermal plot of κ in Figure 14.4 suggests that the transitions take place at constant temperature. Another problem is the continuity of the compressibility parameter. As shown in Figure 14.17, the PVT data replotted as isobaric $V = V(T)$ versus P show that the slopes are continuous across the thick straight line, representing $T_g = T_g(P)$ from Figure 14.13. Thus, for several reasons, the value of dT_g/dP from Eq. (14.9) will not be calculated.

14.5.2 Glassy State of Amorphous Polymers

The analysis of vitreous state data followed the *simplified* procedure, justified by earlier works [Quach and Simha, 1971, 1972; McKinney and Simha, 1974, 1976; Curro et al., 1981; Utracki, 2007a]. The independent variables in the glassy state are indicated by primes (i.e., T' and P'). From the PVT dependencies the hole fraction, $h_{\text{glass}} = h(T', P')$, was calculated by substituting $V = V(T', P')$ into Eq. (14.2), for which the $\langle P^* \rangle$, $\langle T^* \rangle$, and $\langle V^* \rangle$ parameters were known from the $T > T_g$ data. The hole fraction that the melt would have at T' and P' , $h_{\text{extrapol}} = h(T', P')$, was computed from

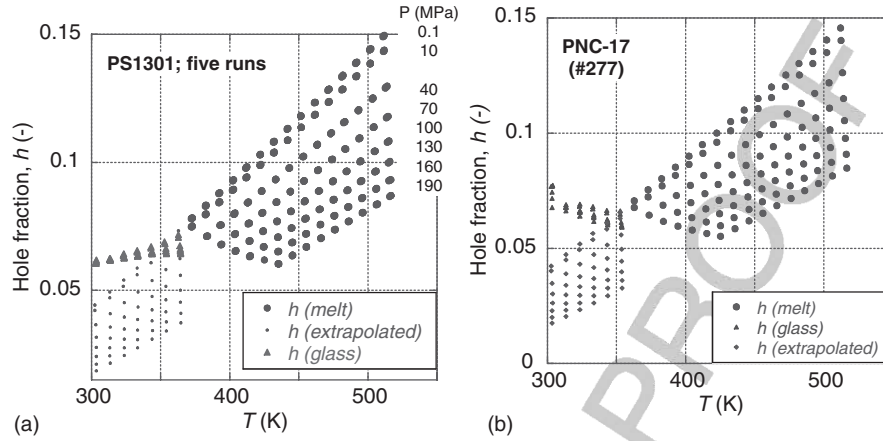


FIGURE 14.18 Hole fraction versus T for (a) PS and (b) PNC-17. Three symbols for h indicate the hole fraction in the melt, in the glass extrapolated from the melt, and computed for the vitreous region.

Eqs. (14.2) and (14.3). As shown in Figure 14.18, the values of h_{glass} are larger than those of h_{extrapol} . The figure illustrates the effects of clay addition on free volume: small in the molten state and dramatic in the glass. Furthermore, whereas in neat polymer, h always increases with increasing temperature, in the highly loaded PNC-17 glass, it decreases at $304 < T(\text{K}) < 314$ (i.e., at $T/T_g \approx 0.86 \pm 0.02$, hence just above T_β).

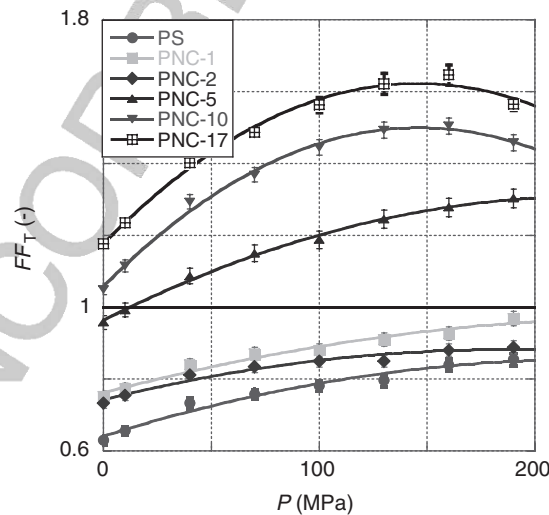
According to Eq. (14.13), for calculating FF_T the slopes $(\partial h / \partial T')_{P, \text{glass}}$ and $(\partial h / \partial T')_{P, \text{extrapol}}$ need to be determined. Because of the initial rapid shrinkage of highly loaded CPNC glasses, for these and ensuing calculations only values for $T > 320 \text{ K}$ were used. The results are listed in Table 14.9 and shown in Figure 14.19. The horizontal line at $FF_T = 1$ separates PS, PNC-1, and PNC-2 with $FF_T < 1$, from PNC-5, PNC-10, and PNC-17 with $FF_T > 1$. This division is readily explained by the presence of free PS matrix below $w_{\text{max}} = 3.6 \text{ wt\% MMT}$, and its absence above this limit. Other solid lines in Figure 14.19 represent the second-order polynomial: $FF_T = \sum a_i P^i$. Since the PVT tests for each material were repeated two to five times, the experimental error of FF_T is 2 to 5%, thus comparable to that reported previously [Utracki, 2007a]. However, while for neat polymers, $FF_T < 0.9$, the high values for CPNCs, $FF_T > 1$, are unprecedented, contradicting its definition as a fraction. As discussed later, the discrepancy originates from the presence of a large amount of molten intercalant entrapped in glassy CPNC.

Figure 14.20 displays the concentration dependence of the a_i parameters at zero pressure of the polynomial: $FF_T = \sum a_i P^i$. The shape of these dependencies also reflects the effect of the free PS disappearance at $w_{\text{max}} \approx 3.6 \text{ wt\% MMT}$. Above this concentration, both functions, FF_T and dFF_T/dP , increase rapidly. The value $FF_{T,P=0} = 0.64 \pm 0.03$ for PS at ambient pressure is comparable to the average obtained for several PS resins (e.g., $FF_{T,P=0} = 0.69 \pm 0.01$).

TABLE 14.9 Free-Volume Frozen Fraction (FF_T) of PS and Its PNC

P (MPa)	PS	PNC-1	PNC-2	CPNC5	PNC-10	PNC-17
0.1	0.62994	0.75220	0.73348	0.9582	1.0507	1.1798
10	0.65665	0.77350	0.75455	0.9927	1.1150	1.2389
40	0.73364	0.83976	0.81262	1.0872	1.2934	1.4030
70	0.75884	0.87018	0.83566	1.1503	1.3686	1.4900
100	0.78189	0.88023	0.85029	1.1877	1.4454	1.5852
130	0.79624	0.91088	0.85015	1.2454	1.4929	1.6513
160	0.84049	0.92701	0.88066	1.2776	1.5044	1.6748
190	0.85584	0.96829	0.88850	1.3028	1.4579	1.5807

Cooled or compressed molten amorphous polymer transforms into glass at the rate-dependent transition temperature: $T_g = T_g(q, P)$ or $T_g = T_g(q, T)$, respectively. The process engenders a variety of structures and affects the free-volume content and its functional dependencies within the glassy state, $h = h(P, T, t_a)$. Evidently, fast quenching freezes more free volume than a slow one. Since the vitreous structure is not at thermodynamic equilibrium, there is a progressive loss of free volume and relaxation of the residual stresses known as *physical aging* [Struik, 1978]. The glass relaxation is most rapid at the midpoint between two transition temperatures, T_g and T_β [i.e., $T_{\max}/T_g = (T_g - T_\beta)/2T_g \approx 0.88 \pm 0.03$]. Thus, for PS-based CPNCs under ambient pressure, the maximum rate of aging is expected at $T_{\max} = 308$ to 318 K. For PS the distribution of the aging rate versus temperature was relatively narrow, spanning about ± 15 K [Struik, 1978].

**FIGURE 14.19** Pressure dependence of the free-volume frozen fraction for PS and its PNC.

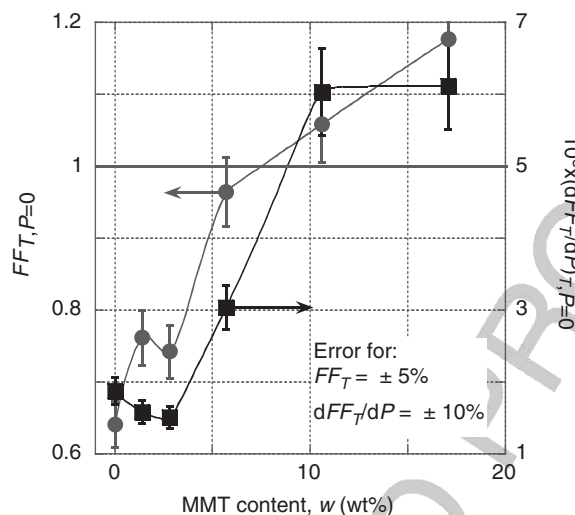


FIGURE 14.20 Zero-pressure values of FF and its derivative, dFF/dP , versus clay content.

Adsorption and solidification of organics on the high-energy clay surface reduces the free volume by equivalence of cooling by about 50°C [Utracki et al., 2003]. However, most CPNCs contain organoclay having low-melting-point intercalant. For example, the discussed PS-based CPNC contains C10A, clay preintercalated with 25% excess of 2MBHTA ($T_m \approx 325$ K) over the cation-exchange capability of MMT. During annealing, which precedes the *PVT* measurements, a large amount of free volume becomes entrapped within the MMT stacks dispersed in the glassy matrix. The high-mobility intercalant molecules plasticize the PS glass, reducing its T_g by about 10°C, as well as increasing the free-volume content, especially at high organoclay loadings. In consequence, at ambient pressure the experimental value of h for PNC-17 in Figure 14.18 is about the same at $T = 303$ K (glass) as at $T = 377$ K (melt). This large amount of free volume is fully entrapped after quenching to room temperature, $RT < T_\beta$.

The *PVT* measurements are relatively slow, as the isothermal scan of eight pressures at the first temperature, T_1 , takes about 47 min, then T_1 is increased by 10°C, and so on. Heating the glass from $RT < T_\beta$ up to T_g induces physical aging seen as a loss of free volume at $T > T_\beta$, which translates into unexpectedly large values of the FF_T . The loss of free volume affects the matrix structure, macromolecular mobility, release of residual stresses, and hence it affects the performance. It is noteworthy that during the aging process the average free-volume cavity size remains constant but their number decreases [Cangialosi et al., 2003, 2005].

In amorphous polymers the physical aging takes place at $T_\beta < T < T_g$ and heating the material to $T \geq T_g + 30^\circ\text{C}$ erases the glassy structure. In semicrystalline polymers, aging is observed not only below T_g but also at $T_g < T < T_m$ [Struik, 1978; Hutchinson, 1995]. Thus, at low temperature the aging affects mainly the glass, while above T_g it causes modification of the crystalline state by recrystallization, crystal growth, and

often changes in the crystalline cell structure. The physical aging usually increases stiffness and brittleness, while the stress release may cause dimensional changes and warping. A phenomenological model of structural relaxation during physical aging was proposed by Narayanaswamy [1971]. The model employs bulk and shear stress relaxation functions and volumetric strain; thus, it may be applied to any material, including CPNC.

Robertson et al. [1984] developed a stochastic model for predicting the kinetics of physical aging of polymer glasses. The equilibrium volume at a given temperature, the hole fraction, and the fluctuations in free volume were derived from the S-S cell-hole theory. The rate of volume changes was assumed to be related to the local free volume content; thus, it varied from one region to the next according to a probability function. The model predictions compared favorably with the results from Kovacs' laboratory. Its evolution and recent advances are discussed by Simha and Robertson in Chapter 4.

One of the first studies of PNC physical aging was published by Lee and Lichtenhan [1998] for epoxy containing $w = 0$ to 9 wt% of polyhedral oligomeric silsesquioxane (POSS). The presence of POSS increased T_g and the relaxation time; thus, the nanofiller slowed down the molecular dynamics. For amorphous polymers at $T_\beta \leq T \leq T_g$, Kozlov et al. [1999, 2004] developed the structural cluster model. The cluster volume fraction depends on temperature:

$$\phi_{cl} = 1 - \phi_m = \lambda(T_g - T)^\gamma \quad (14.22)$$

where λ and $\gamma < 1$ are equation parameters. The authors postulated that aging increases the cluster content, ϕ_{cl} , up to a quasiequilibrium level, characteristic for the aging temperature and controlled by the entropy-related polymer chain tension.

A Ph.D. thesis and a series of publications described the preparation and properties (including the physical aging) of the PA-6- or PA-66-based CPNC and their fiber-reinforced composites [Vlasveld, 2005; Vlasveld et al., 2005a-c]. Thus, creep at constant stress of $\sigma = 16$ MPa was measured at room temperature for about 2.5 hrs after aging time, $t_a \leq 820$ hours. Among the CPNC samples studied there was a commercial M1030D from Unitika [PA-6 polymerized in the presence of 4.6 wt% of synthetic sodium fluoromica (FM)] as well as CPNC prepared by melt compounding FM with low-molecular-weight PA-6 ($M_n = 16$ kg/mol). The physical aging was expressed in terms of the double-logarithmic shift rate:

$$\mu \equiv \left(\frac{\partial \log a_{t_a}}{\partial \log t_a} \right)_{T, \sigma} \quad (14.23)$$

where a_{t_a} is the creep shift factor after aging for t_a at constant temperature and stress, σ . While for PA-6 with $M_n = 16$ and 36 kg/mol the shift rate was $\mu = 0.70$ and 0.76, respectively, for compounded CPNC it ranged from 0.82 to 0.84. The largest shift rate, $\mu = 0.93$, was obtained for M1030D; addition of 5 wt% clay reduced the creep compliance by up to 80% [Vlasveld et al., 2005b]. The superiority of this commercial CPNC might originate in better exfoliation and preservation of the clay

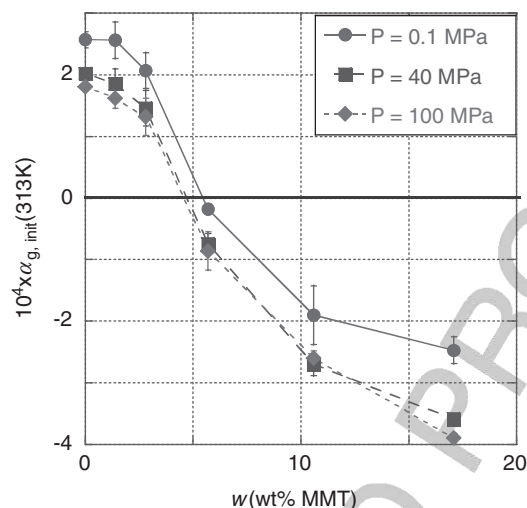


FIGURE 14.21 Initial thermal expansion coefficient of glassy PS and its CPNC versus MMT content. The value was calculated from Eq. (14.1) using isobaric data at 303 to 323 K.

high aspect ratio ($p > 5000$) achieved during polymerization than those obtained in melt compounding. Thus, incorporation of FM into PA matrix significantly reduced the creep compliance and the rate of physical aging. Furthermore, the CPNC modulus increased with nanofiller dispersion, clay content, and aging time.

Physical aging of PNC thin films, prepared by solution blending of PS, PMMA, or poly(2-vinylpyridine) (P2VP) with silica (SiO_2 , diameter $D = 10$ to 15 nm) or alumina (Al_2O_3 , $D = 47$ nm) nanoparticles, was studied by Rittigstein and Torkelson [2006]. The reduction of the physical aging rate, μ , for the P2VP with 4 vol% alumina particles was the largest (by a factor of 17). The authors observed that increased T_g parallels the reduction of μ , concluding that if a PNC is to be stable or nearly impervious to aging, it must comprise well-dispersed nanoparticles possessing strong attractive interactions with the matrix.

In the following publication from the same laboratory, the physical aging of PMMA or PS with SiO_2 nanoparticles ($D = 10$ to 15 nm) was studied by means of fluorescence and dielectric spectroscopy [Priestley et al., 2007]. Addition of 0.4 vol% of silica reduced μ by a factor of 20. At the same time, due to hydrogen bonding of PMMA ester groups to hydroxyl groups on the silica surface, the strength of the dielectric β relaxation was reduced by about 50%. In the absence of hydrogen bonding in the PS/silica system, no reduction of μ was observed. The dielectric spectroscopy showed that the addition of nanoparticles caused T_g to increase and, at the same time, T_β to decrease; the intensity of the loss peak also decreased.

The presence of clay platelets during quenching leads to entrapment of excess free volume and locking the structure, which reduces the postprocessing dimensional changes. The PVT data analysis of the PS-C10A suggests that large quantities of free volume are entrapped in samples containing $w > 3.6$ wt% MMT; thus, annealing might be required for obtaining the highest stiffness at clay loading below this critical

concentration. Since during the *PVT* measurements the temperature increases with increasing test time, in the absence of direct measurements of the rate of physical aging, Figure 14.21 might be considered a qualitative indicator. The figure displays the thermal expansion coefficient of glassy PS and its CPNC, $\alpha_{g,init}$, as a function of pressure and MMT content at the beginning of the test (notably, a plot of the low- T temperature gradient, dh_g/dT , versus w shows nearly identical dependence). The values were determined at $303 \leq T(K) \leq 323$ for $P = 0.1, 40$, and 100 MPa; within the limits of experimental error the three isobars are alike. The $\alpha_{g,init}$ coefficient is positive and nearly constant for $w \leq 1.4$ wt% MMT. With increasing organoclay content the amount of free volume entrapped increases and the effect of its release increases, causing $\alpha_{g,init}$ to decrease toward large negative values. Thus, at high MMT content, $w > 3.6$ wt%, the specimen shrinks on heating ($\alpha_{g,init} < 0$). Contrary to the observation by Rittigstein and Torkelson [2006], in PS/C10A systems T_g decreases with increasing w (see Table 14.8), and the effects of physical aging increase.

14.6 SUMMARY AND CONCLUSIONS

The *PVT* behavior in the molten and glassy states of PS-based CPNC containing 0 to 17.1 wt% MMT was examined using the Simha–Somcynsky equation of state. The theory provided an excellent fit to the *PVT* surface at $T > T_g$ with ± 0.0003 -mL/g residuals of specific volume. From the fitting, the bulk-average characteristic reducing parameters, $\langle P^* \rangle$, $\langle V^* \rangle$, and $\langle T^* \rangle$, and the Lennard-Jones (L-J) interaction quantities, $\langle \epsilon^* \rangle$ and $\langle v^* \rangle$, were calculated. In addition, the free-volume function, $h = h(V, T)$, was computed. Considering the presence of a solidified polymer layer on the intercalated layer predicted that molten PS (“free” PS) disappears at $w_{max} \approx 3.6$ wt% MMT; several experimental quantities had local extrema near this composition (i.e., L-J parameters, α_m , relative loss of free volume, Δh , etc.). Assuming a binary structure for the CPNC (i.e., a PS matrix with dispersed organoclay stacks surrounded by solidified PS), the individual interaction parameters ϵ_{ij}^* and v_{ij}^* for polymer ($ij = 11$), for stacks ($ij = 22$), and for stack–polymer ($ij = 12$) were calculated.

Two functions characterize the glass transition region: the glass transition temperature, T_g , and associated with it the free-volume parameter, $h_g = h(T_g)$. They both depend on pressure, P , and MMT content, w . Thus, T_g increases with P and decreases with w , whereas h_g decreases with P and w . These decreases with increasing organoclay loading indicate plasticization of PS by the 2MBHTA intercalant and absence of direct bonding between the MMT surface and PS macromolecules. The pressure gradients of these functions also showed local extrema at $w_{max} = 3.6$ wt% MMT.

In the vitreous region the V versus T slope depends on P and the MMT content; for PS resins it is positive, but as P and the clay content increase, its value decreases toward negative. In consequence, the apparent free-volume frozen fraction, FF_T , changes from about 0.6 for PS to 1.6 for PNC-17 at 160 MPa. The value of FF at ambient pressure, $FF_{P=0.1}$, and its first derivative with respect to P also show local extrema at the concentration of free PS disappearance, w_{max} .

The thermal expansion coefficient, α , and the compressibility coefficient, κ , depend on T , P , and w . The former decreased with P ; its concentration dependence in the

molten state is slight, but in the vitreous state it changes with w , going through a local extremum at $w_{\max} = 3.6$ wt%. The compressibility parameter was the most informative, indicating the presence of two secondary transitions, one below and the other above T_g . It is noteworthy that for these PS-based CPNC only at $T/T_g > 1.2 \pm 0.1$ was a monotonic increase of κ with T observed. In plots of κ versus T , the transition region, **T**, stretched from the P -independent $T_{g,P=0}$ to $T_T \approx 1.2T_g$. The data indicate that with the growing clay content the free volume in the vitreous state increases and the physical aging effects become increasingly important. There are two sources for the unusually large free-volume content in the glassy region: the free-volume fraction of the polymeric matrix frozen at T_g and that entrapped by the PS glass free volume of the 2MBHTA intercalant with low melting point, $T_m \approx 325$ K.

There are significant differences in the PVT and the derivative properties of the amorphous and semicrystalline polymers, extended to their CPNC. Thus, whereas in PS there is a large transient region on both sides of the main (glass) transition; in PA-6 the main transition (melting) is relatively narrow. For amorphous systems the analysis is based on the Simha–Somcynsky equation of state, for both the melt and the glass; while for semicrystalline systems the S–S equation of state is used for the molten and supercooled liquid phases and the Midha–Nanda–Simha–Jain (MNSJ) equation of state is used for the crystalline phase dispersed in the supercooled phase at $T_g \leq T \leq T_m$. The theoretical analysis of this “solid” phase yields the crystalline content, which increases with pressure and varies nonlinearly with clay content. The derivatives, $\alpha = \alpha(T, P)$ and $\kappa = \kappa(T, P)$, show surprisingly different behavior: Whereas the isobaric values of κ increased in the solid and molten phases following a second-order curve, α was discontinuous at T_m , having higher values below the transition temperature than above. The mechanism responsible for such behavior may be related to the free-volume increase caused by premelting.

Acknowledgments

The author thanks Robert Simha and Gunter Dlubek, as well as Kenneth Cole, for reviewing this chapter and for fruitful discussions and suggestions for improvement.

REFERENCES

- Angell, C. A., in *Relaxation in Complex Systems*, Ngai, K. L., and Wright, G. B., Eds., NRL, Washington, DC, 1985.
- Angell, C. A., Formation of glasses from liquids and biopolymers, *Science*, **267**, 1924–1935 (1995).
- Bamji, S. S., Abou-Dakka, M., Bulinski, A. T., Utracki, L., and Cole, K., Dielectric properties of propylene containing nano-particles, in *Proceedings of the 74th IEEE Conference on Electrical Insulation and Dielectric Phenomena (CEIDP)*, Nashville, TN, Oct. 16–19, 2005, pp. 166–170.
- Bartoš, J., and Krištiak, J., Free volume aspects of the strong–fragile classification of polymer liquids, *J. Non-Cryst. Solids*, **235–237**, 293–295 (1998).

- Bartoš, J., Krištiak, J., Šauša, O., Bandžuch, P., and Zrubcová, J., Experimental free volume aspect of the polymer rheology as obtained by positron annihilation lifetime spectroscopy, *Macromol. Symp.*, **158**, 111–123 (2000).
- Bicerano, J., in *Encyclopedia of Polymer Science and Technology*, 3rd ed., Mark, H.F., Ed., Wiley, Hoboken, NJ, 2003.
- Binder, K., Baschnagel, J., and Paul, W., Glass transition of polymer melts: test of theoretical concepts by computer simulation, *Prog. Polym. Sci.*, **28**, 115–172 (2003).
- Böhmer, R., Ngai, K. L., Angell, C., and Plazek, D., Nonexponential relaxations in strong and fragile glass formers, *J. Chem. Phys.*, **99**, 4201–4209 (1993).
- Boyer, R. F., in *Encyclopedia of Polymer Science and Technology*, Suppl. Vol. **2**, Mark, H. F., Ed., Wiley, New York, 1977, pp. 745–839.
- Boyer, R. F., Dynamics and thermodynamics of the liquid state ($T > T_g$) of amorphous polymers, *J. Macromol. Sci. Phys.*, **B18** (3), 461–553 (1980).
- Boyer, R. F., in *Polymer Yearbook*, Vol. **2**, Pethrick, R. A., Ed., Harwood Academic, New York, 1985.
- Boyer, R. F., in *Order in the Amorphous State*, Miller, R. L., and Rieke, J. K., Eds., Plenum Press, New York, 1987.
- Briatico-Vangosa, F., and Rink, M., Dilatometric behavior and glass transition in a styrene–acrylonitrile copolymer, *J. Polym. Sci. B*, **43**, 1904–1913 (2005).
- Bueche, F., *Physical Properties of Polymers*, Interscience, New York, 1962, pp. 85–110.
- Buhot, A., and Garrahan, J. P., Crossover from fragile to strong glassy behaviour in the spin facilitated chain model, *J. Phys. Condens. Matter*, **14**, 1499–1507 (2002).
- Cangialosi, D., Schut, H., van Veen, A., and Picken, S. J., Positron annihilation lifetime spectroscopy for measuring free volume during physical aging of polycarbonate, *Macromolecules*, **36**, 142–147 (2003).
- Cangialosi, D., Wübbenhorst, M., Schut, H., and Picken, S. J., Relaxation of free volume in polycarbonate and polystyrene studied by positron annihilation lifetime spectroscopy, *Acta Phys. Polon. A*, **107**, 690–696 (2005).
- Casalini, R., and Roland, C. M., Scaling of the supercooled dynamics and its relation to the pressure dependence of the dynamic crossover and the fragility of glass formers, *Phys. Rev. B*, **71**, 014210 (2005).
- Clausius, R., Über das Verhalten der Kohlensäure in Bezug auf Druck, Volumen und Temperatur, *Ann. Phys. Chem.*, **IX**, 337–359 (1880).
- Cosgrove, T., Heath, T. G., Ryan, K., and Crowley, T. L., Neutron scattering from adsorbed polymer layers, *Macromolecules*, **20**, 2879–2882 (1987).
- Cosgrove, T., Heath, T. G., Phipps, J. S., and Richardson, R. M., Neutron reflectivity studies of polymer adsorbed on mica from solution, *Macromolecules*, **24**, 94–98 (1991).
- Cowie, J. M. G., McEwen, I. J., and McIntyre, R., in *Polymer Blends Handbook*, Utracki, L. A., Ed., Kluwer Academic, Dordrecht, The Netherlands, 2002.
- Curro, J. G., Polymeric equations of state, *J. Macromol. Sci. Rev. Macromol. Chem.*, **C11**, 321–366 (1974).
- Curro, J. G., Lagasse, R. R., and Simha, R., Use of a theoretical equation of state to interpret time-dependent free volume in polymer glass, *J. Appl. Phys.*, **52**, 5892–5897 (1981).
- Debenedetti, P. G., and Stillinger, F. H., Supercooled liquids and the glass transition, *Nature*, **410**, 259–267 (2001).

- Dlubek, G., Fluctuation approach for the estimation of the dynamic heterogeneity in glass-forming liquids from the dispersion in *o*-Ps lifetimes: free volume fluctuations in polymers, *J. Non-Cryst. Solids*, **352**, 2869–2979 (2006).
- Dlubek, G., Personal communication, Jan. 2008.
- Dlubek, G., Saarinen, K., and Fretwell, H. M., The temperature dependence of the local free volume in polyethylene and polytetrafluoroethylene: a positron lifetime study, *J. Polym. Sci. B*, **36**, 1513–1528 (1998).
- Dlubek, G., Kilburn, D., Bondarenko, V., Pionteck, J., Krause-Rehberg, R., and Alam, M. A., Characterization of free volume in amorphous materials by PALS in relation to relaxation phenomena, in *24th Arbeitskreistagung 'Nichtkristalline Strukturen' of DGK, Jena, Germany, Sept. 2003*.
- Dlubek, G., Bondarenko, V., Kilburn, D., Al-Qaradawi, I. Y., Kilburn, D., and Krause-Rehberg, R., The structure of the free volume in poly(styrene-co-acrylonitrile) from positron lifetime and pressure–volume–temperature (PVT) experiments, *Macromol. Chem. Phys.*, **205**, 500–522 (2004).
- Dlubek, G., Hassan, E. M., Pionteck, J., and Krause-Rehberg, R., The free volume of an epoxy resin and its relation to the structural relaxation: evidence from positron lifetime and pressure–volume–temperature experiments, *Phys. Rev. E*, **73**, 031803 (2006).
- Dlubek, G., Shaikh, M. Q., Krause-Rehberg, R., and Paluch, M., The effect of free volume and temperature on the structural relaxation in polymethylphenylsiloxane: a positron lifetime and pressure–volume–temperature study, *J. Chem. Phys.*, **126**, 024906 (2007).
- Eisenberg, A., and Shen, M. C., Recent advances in glass transitions in polymers, *Rubber Chem. Technol.*, **43**, 156–170 (1970).
- Fleer, G., Cohen-Stuart, M. A., Scheutjens, J. M. H. M., Cosgrove, T., and Vincent, B., *Polymers at Interfaces*, Chapman Hall, London, 1993.
- Flory, P. J., *Statistical Mechanics of Chain Molecules*, Interscience, New York, 1969, Chap. V.
- Frisk, P., and Laurent, J., Nanocomposite polymer container, WO 98/01346, Jan. 15, 1998, to Tetra Laval Holdings & Finance, SA.
- Frost & Sullivan, materials.frost.com/, 2008.
- Garboczi, E. J., Snyder, K. A., Douglas, J. F., and Thorpe, M. F., Geometrical percolation threshold of overlapping ellipsoids, *Phys. Rev. E*, **52**, 819–828 (1995).
- Goliath Business Knowledge on Demand, *Polymer Nanocomposites Report 2006*; BCC Research, *Polymer Nanocomposites: Nanoparticles, Nanoclays and Nanotubes*. Report NAN021B, 2004.
- Götze, W., Recent tests of the mode-coupling theory for glassy dynamics, *J. Phys. Condens. Matter*, **11**, A1–A45 (1999).
- Götze, W., and Sjögren, L., Scaling properties in supercooled liquids near the glass transition, *J. Phys. C*, **21**, 3407–3421 (1988).
- Götze, W., and Sjögren, L., Relaxation processes in supercooled liquids, *Rep. Prog. Phys.*, **55**, 241–376 (1992).
- Götze, W., and Sjögren, L., The mode coupling theory of structural relaxations, *Transp. Theory Stat. Phys.*, **24**, 801–853 (1995).
- Han, S. J., Lohse, D. J., Condo, P. D., and Sperling, L. H., Pressure–volume–temperature properties of polyolefin liquids and their melt miscibility, *J. Polym. Sci. B*, **37**, 2835–2844 (1999).

- Hentschke, R., Molecular modeling of adsorption and ordering at solid interfaces, *Macromol. Theory Simul.*, **6**, 287–316 (1997).
- Higuchi, H., and Simha, R., Free volume quantities and gas diffusion properties at low temperatures, *Macromolecules*, **29** (8), 3030–3031 (1996).
- Hirschfelder, J. O., Curtis, C. F., and Bird, R. B., *Molecular Theory of Gases and Liquids*, Wiley, New York, 1954.
- Hofmann, A. W., Beiträge zur Kenntnifs der flüchtigen organischen Basen; X. Uebergang der flüchtigen Basen in eine Reihe nichtflüchtiger Alkaloi de, *Liebigs Ann. Chem.*, **78**, 253–286 (1851).
- Horn, R. G., and Israelachvili, J. N., Molecular organization and viscosity of a thin film of molten polymer between two surfaces as probed by force measurements, *Macromolecules*, **21**, 2836–2841 (1988).
- Hu, H.-W., and Granick, S., Viscoelastic dynamics of confined polymer melts, *Science*, **258**, 1339–1342 (1992).
- Hutchinson, J. M., Physical aging of polymers, *Prog. Polym. Sci.*, **20**, 703–760 (1995).
- Israelachvili, J. N., Tirrell, M., Klein, J., and Almog, Y., Forces between two layers of adsorbed polystyrene immersed in cyclohexane below and above the Θ -temperature, *Macromolecules*, **17**, 204–209 (1984).
- Jäckle, J., Models of the glass transition, *Rep. Prog. Phys.*, **49**, 171–231 (1986).
- Jain, R. K., and Simha, R., On the statistical thermodynamics of multicomponent fluids: equation of state, *Macromolecules*, **13**, 1501–1508 (1980).
- Jain, R. K., and Simha, R., Statistical thermodynamics of multicomponent fluids, *Macromolecules*, **17**, 2663–2668 (1984).
- Jain, R. K., Simha, R., and Zoller, P., Theoretical equation of state of polymer blends: the poly(2,6-dimethyl-1,4-phenylene ether)–polystyrene pair, *J. Polym. Sci. Polym. Phys. Ed.*, **20**, 1399–1408 (1982).
- Kanaya, T., and Kaji, K., Dynamics in the glassy state and near glass transition temperature of amorphous polymers as studied by neutron scattering, *Adv. Polym. Sci.*, **154**, 87–141 (2001).
- Kawasaki, K., Correlation-function approach to the transport coefficients near the critical point, *Phys. Rev.*, **150**, 291–306 (1966).
- Kilburn, D., Dlubek, G., Pionteck, J., and Alam, M. A., Free volume in poly(*n*-alkyl methacrylate)s from positron lifetime and *PVT* experiments and its relation to the structural relaxation, *Polymer*, **47**, 7774–7785 (2006a).
- Kilburn, D., Wawryszczuk, J., Dlubek, G., Pionteck, J., Hassler, R., and Alam, M. A., Temperature and pressure dependence of the free volume in polyisobutylene from positron lifetime and pressure–volume–temperature experiments, *Macromol. Chem. Phys.*, **207**, 721–734 (2006b).
- Kim, S. H., Chung, J. W., Kang, T. J., Kwak, S.-Y., and Suzuki, T., Determination of the glass transition temperature of polymer/layered silicate nanocomposites from positronium annihilation lifetime measurements, *Polymer*, **48**, 4271–4277 (2007).
- Kisliuk, A., Mathers, R. T., and Sokolov, A. P., Crossover in dynamics of polymer liquids, *J. Polym. Sci. Polym. Phys. Ed.*, **38**, 2785–2790 (2000).
- Kovacs, A. J., La contraction isotherme du volume des polymères amorphes, *J. Polym. Sci.*, **30**, 131–147 (1958).
- Kovacs, A. J., and Hutchinson, J. M., Isobaric thermal behavior of glasses during uniform cooling and heating: dependence of the characteristic temperatures on the relative contributions

- of temperature and structure to the rate of recovery: II. A one-parameter model approach, *J. Polym. Sci. Polym. Phys. Ed.*, **17**, 2031–2058 (1979).
- Kozlov, G. V., Beloshenko, V. A., Varyukin, V. N., and Lipatov, Yu. S., Application of cluster model for the description of epoxy polymer structure and properties, *Polymer*, **40**, 1045–1051 (1999).
- Kozlov, G. V., Dolbin, I. V., and Zaikov, G. E., Theoretical description of physical aging of amorphous polymers, *Russ. J. Appl. Chem.*, **77**, 267–270 (2004).
- Lakoma, I., and Merilkon, O., Thomson Business Intelligence, Nanotechnology market studies—what do they tell us? www.nanoharju.fi/Iikka%20Lakoma.pdf, Nov. 23, 2005.
- Lambert, S. M., Song, Y., and Prausnitz, J. M., Equations of state for polymer systems, in *Equations of State for Fluids and Fluid Mixtures*, Sengers, J. V., Kayser, R. F., Peters, C. J., and White, H. J., Eds., Elsevier, Amsterdam, 2000, pp. 523–588.
- Lee, A., and Lichtenhan, J. D., Viscoelastic responses of polyhedral oligosilsesquioxane reinforced epoxy systems, *Macromolecules*, **31**, 4970–4974 (1998).
- Li, G., Leung, S. N., Hasan, M. M., Wang, J., Park, C. B., and Simha, R., A thermodynamic model for ternary mixture systems: gas blends in a polymer melt, *Fluid Phase Equilibria*, **266** (1–2), 129–142 (2008).
- Luengo, G., Schmitt, F.-J., Hill, R., and Israelachvili, J. N., Thin film rheology and tribology of confined polymer melts: contrasts with bulk properties, *Macromolecules*, **30**, 2482–3492 (1997).
- Maier, T. R., Jamieson, A. M., and Simha, R., Phase equilibria in SBR/polybutadiene elastomer blends: application of Flory–Huggins theory, *J. Appl. Polym. Sci.*, **51** (6), 1053–1062 (1994).
- McKinney, J. E., and Simha, R., Configurational thermodynamic properties of polymer liquids and glasses: poly(vinyl acetate), *Macromolecules*, **7**, 894–901 (1974); *ibid.*, **9**, 430–441 (1976); *J. Res. NBS Phys. Chem.*, **81A**, 283–297 (1977).
- Mercier, J. P., and Aklonis, J. J., Glass transition temperature: What does it measure? What does it mean? *J. Paint Technol.*, **43**, 44–49 (1971).
- Murthy, S. S. N., The nature of decoupling of various relaxation processes in glass-forming liquids, *J. Mol. Liq.*, **44**, 211–230 (1990).
- Murthy, S. S. N., Liquid–liquid transition in polymers and glass-forming liquids, *J. Polym. Sci. B*, **31**, 475–480 (1993).
- Murthy, S. S. N., and Kumar, D., Glass formation in organic binary liquids studied using differential scanning calorimetry, *J. Chem. Soc. Faraday Trans.*, **1993** (14), 2423–2427 (1993).
- Narayanaswamy, O. S., Model of structural relaxation in glass, *J. Am. Ceram. Soc.*, **54**, 491–498 (1971).
- Nelson, J. K., Reed, C. W., Utracki, L. A., and MacCrone, R., Role of the interface in determining the dielectric properties of nanocomposites, in *2004 IEEE Conference on Electrical Insulation and Dielectric Phenomena*, Boulder, CO, Oct. 17–20, 2004, pp. 314–317.
- Ngai, K. L., Dynamic and thermodynamic properties of glass-forming substances, *J. Non-Cryst. Solids*, **275**, 7–51 (2000).
- Ngai, K. L., An extended coupling model description of the evolution of dynamics with time in supercooled liquids and ionic conductors, *J. Phys. Condens. Matter*, **15**, S1107–S1125 (2003).

- Okada, A., and Usuki, A., Twenty years of polymer–clay nanocomposites, *Macromol. Mater. Eng.*, **291**, 1449–1476 (2006).
- Papazoglou, E., Simha, R., and Maurer, F. H. J., Thermal expansivity of particulate composites: interlayer versus molecular model, *Rheol. Acta*, **28**, 302–308 (1989).
- Patterson, G. D., Bair, H. E., and Tonelli, A. E., Thermal behavior of atactic polystyrene above the glass–rubber relaxation, *J. Polym. Sci. Polym. Symp. Ed.*, **54**, 249–257 (1976).
- Paul, W., Molecular dynamics simulations of the glass transition in polymer melts, *Polymer*, **45**, 3901–3905 (2004).
- Priestley, R. D., Rittigstein, P., Broadbelt, L. J., Fukao, K., and Torkelson, J. M., Evidence for the molecular-scale origin of the suppression of physical ageing in confined polymer: fluorescence and dielectric spectroscopy studies of polymer–silica nanocomposites, *J. Phys. Condens. Matter*, **19**, 205120 (2007).
- Prigogine, I., Bellemans, A., and Mathot, V., *The Molecular Theory of Solutions*, North-Holland, Amsterdam, 1957.
- Quach, A., and Simha, R., Pressure–volume–temperature properties and transitions of amorphous polymers; polystyrene and poly(orthomethylstyrene), *J. Appl. Phys.*, **42**, 4592–4606 (1971).
- Quach, A., and Simha, R., Statistical thermodynamics of the glass transition and the glassy state of polymers, *J. Phys. Chem.*, **76**, 416–421 (1972).
- Rao, K. J., Kumar, S., and Bhat, M. H., A chemical approach to understand fragilities of glass-forming liquids, *J. Phys. Chem. B*, **105** (38), 9023–9027 (2001).
- Reichman, D. R., and Charbonneau, P., Mode-coupling theory, *J. Stat. Mech. Theory Exp.*, P05013 (2005).
- Rittigstein, P., and Torkelson, J. M., Polymer–nanoparticle interfacial interactions in polymer nanocomposites: confinement effects on glass transition temperature and suppression of physical aging, *J. Polym. Sci. B*, **44**, 2935–2943 (2006).
- Robertson, R. E., Simha, R., and Curro, J. G., Free volume and the kinetics of aging of polymer glasses, *Macromolecules*, **17**, 911–919 (1984).
- Rodgers, P. A., Pressure–volume–temperature relationships for polymeric liquids, *J. Appl. Polym. Sci.*, **50**, 1061–1080, 2075–2083 (1993).
- Roe, R.-J., in *Encyclopedia of Polymer Science and Technology*, 2nd ed., Vol. 7, Mark, H. F., Ed., Wiley, New York, 1987, pp. 531–544.
- Rudolf, B., Kressler, J., Shimomami, K., Ougizawa, T., and Inoue, T., Evaluation of equation-of-state parameters from PVT data, *Acta Polym.*, **46**, 312–318 (1995).
- Rudolf, B., Ougizawa, T., and Inoue, T., Evaluation of equation-of-state parameters and the description of PVT-data, *Acta Polym.*, **47**, 520–524 (1996).
- Scherrer, P., Bestimmung der Größe und der inneren Struktur von Kolloidteilchen mittels Röntgenstrahlen, *Göttinger Nachr., Math. Phys.*, **2**, 98–100 (1918).
- Schmidt, M., Macroscopic volume and free volume of polymer blends and pressure-densified polymers, Ph.D. dissertation, Chalmers University, Göteborg, 2000.
- Schmidt, M., and Maurer, F. H. J., Pressure–volume–temperature properties and free volume parameters of PEO/PMMA blends, *J. Polym. Sci. B*, **36**, 1061–1080 (1998).
- Schmidt, M., and Maurer, F. H. J., Relation between free-volume quantities from PVT-EOS analysis and PALS, *Polymer*, **41**, 8419–8424 (2000).

- Simha, R., and Jain, R. K., Statistical approach for polymer melt composites: bulk modulus and thermal expansivity, in *Society of Plastics Engineers, National Technical Conference Proceedings*, (1982), pp. 78–81.
- Simha, R., and Jain, R. K., Statistical thermodynamics of blends: equation of state and phase relations, *Polym. Eng. Sci.*, **24** (17), 1284–1290 (1984).
- Simha, R., and Moulinié, P., Statistical thermodynamics of gas solubility in polymers, in *Polymer Foams*, Lee, T. S., Ed., Technomic, Lancaster, PA, 2000.
- Simha, R., and Somcynsky, T., On the statistical thermodynamics of spherical and chain molecule fluids, *Macromolecules*, **2**, 342–350 (1969).
- Simha, R., and Xie, H., Applying lattice-hole theory to gas solubility in polymers, *Polym. Bull.*, **40**, 329–335 (1998).
- Simha, R., Wilson, P. S., and Olabisi, O., Pressure-volume-temperature properties of amorphous polymers: empirical and theoretical predictions, *Kolloid Z. Z. Polym.*, **251**, 402–408 (1973).
- Simha, R., Jain, R. K., and Jain, S. C., Bulk modulus and thermal expansivity of melt polymer composites: statistical versus macro-mechanics, *Polym. Compos.*, **5** (1), 3–10 (1982).
- Simha, R., Jain, R. K., and Jain, S. C., Bulk modulus and thermal expansivity of melt polymer composites: statistical versus macro-mechanics, *Polym. Compos.*, **5**, 3–10 (1984).
- Simha, R., Jain, R. K., and Maurer, F. H. J., Bulk modulus of particulate composites: a comparison between statistical and micro-mechanical approach, *Rheol. Acta*, **25**, 161–165 (1986).
- Simha, R., Papazoglou, E., and Maurer, F. H. J., Thermal expansivity and bulk modulus of polymer composites: experiment versus theory, *Polym. Compos.*, **10**, 409–413 (1989).
- Simha, R., Utracki, L. A., and Garcia-Rejon, A., Pressure-volume-temperature relations of a poly- ϵ -caprolactam and its nanocomposite, *Compos. Interfaces*, **8**, 345–353 (2001).
- Somcynsky, T., and Simha, R., Hole theory of liquids and glass transition, *J. Appl. Phys.*, **42**, 4545–4548 (1971).
- Srithawatpong, R., Peng, Z. L., Olson, B. G., Jamieson, A. M., Simha, R., McGervey, J. D., Maier, T. R., and Ishida, H., Positron annihilation lifetime studies of changes in free volume on cross-linking *cis*-polyisoprene, high-vinyl polybutadiene, and their miscible blends, *J. Polym. Sci. B*, **37** (19), 2754–2770 (1999).
- Struik, L. C. E., *Physical Aging in Amorphous Polymers and Other Materials*, Elsevier, Amsterdam, 1978.
- Tanaka, G., and Goettler, L. A., Predicting the binding energy for nylon 6,6/clay nanocomposites by molecular modeling, *Polymer*, **43**, 541–553 (2002).
- Tanoue, S., Utracki, L. A., Garcia-Rejon, A., Tatibouët, J., Cole, K. C., and Kamal, M. R., Melt compounding of different grades of polystyrene with organoclay: Part 1. Compounding and characterization, *Polym. Eng. Sci.*, **44**, 1046–1060 (2004a).
- Tanoue, S., Utracki, L. A., Garcia-Rejon, A., Sammut, P., Ton-That, M.-T., Pesneau, I., Kamal, M. R., and Lyngaae-Jørgensen, J., Melt compounding of different grades polystyrene with organoclay: Part 2. Rheological properties, *Polym. Eng. Sci.*, **44**, 1061–1076 (2004b).
- Tanoue, S., Utracki, L. A., Garcia-Rejon, A., Tatibouët, J., and Kamal, M. R., Melt compounding of different grades of polystyrene with organoclay: Part 3. Mechanical properties, *Polym. Eng. Sci.*, **45**, 827–837 (2005).
- Tarjus, G., Kivelson, S. A., Nussinov, Z., and Viot, P., The frustration-based approach of super-cooled liquids and the glass transition: a review and critical assessment, *J. Phys. Condens. Matter*, **17**, R1143–R1182 (2005).

- Termonia, Y., Monte Carlo modeling of dense polymer melts near nanoparticles, *Polymer*, **50**, 1062–1066 (2009).
- Utracki, L. A., Clay-Containing Polymeric Nanocomposites, 2-vol. monograph, RAPRA, Shawbury, UK, 2004.
- Utracki, L. A., Pressure–volume–temperature dependencies of polystyrenes, *Polymer*, **46**, 11548–11556 (2005).
- Utracki, L. A., Pressure–volume–temperature of molten and glassy polymers, *J. Polym. Sci. B*, **45**, 270–285 (2007a).
- Utracki, L. A., Interphase between nanoparticles and molten polymeric matrix: pressure–volume–temperature measurements, *Compos. Interfaces*, **14**, 229–242 (2007b).
- Utracki, L. A., Mechanical properties of clay-containing polymeric nanocomposites, in Handbook of Polymer Nanocomposites, Gupta, R., Kennel, E., and Kim, K.-J., Eds., CRC Press, Boca Raton, FL, 2008a.
- Utracki, L. A., Polymeric nanocomposites: compounding and performance, *J. Nanosci. Nanotechnol.*, **8**, 1582–1596 (2008b).
- Utracki, L. A., Free volume of molten and glassy polystyrene and its nanocomposites, *J. Polym. Sci. B*, **46**, 2504–2518 (2008c).
- Utracki, L. A., Equation of state of polyamide-6 and its nanocomposites: 1. Fundamentals and the matrix, *J. Polym. Sci. B*, **47**, 299–313 (2009a).
- Utracki, L. A., Equation of state of polyamide-6 and its nanocomposites: 2. Effects of clay, *J. Polym. Sci. Part B: Polym. Phys.*, **47**, 966–980 (2009).
- Utracki, L. A., PVT of amorphous and crystalline polymers and their nanocomposites, *Polym. Degrad. Stab.*, **95**, 411–421 (2010).
- Utracki, L. A., and Lyngaae-Jørgensen, J., Dynamic melt flow of nanocomposites based on poly- ϵ -caprolactam, *Rheol. Acta*, **41**, 394–407 (2002).
- Utracki, L. A., and Sedlacek, T., Free volume dependence of polymer viscosity, *Rheol. Acta*, **46**, 479–494 (2007).
- Utracki, L. A., Sepehr, M., and Li, J., Melt compounding of polymeric nanocomposites, *Int. Polym. Process.*, **21**, 3–16 (2006).
- Utracki, L. A., and Simha, R., Analytical representation of solutions to lattice–hole theory, *Macromol. Chem. Phys. Mol. Theory Simul.*, **10**, 17–24 (2001a).
- Utracki, L. A., and Simha, R., Free volume and viscosity of polymer-compressed gas mixtures during extrusion foaming, *J. Polym. Sci. B*, **39**, 342–362 (2001b).
- Utracki, L. A., and Simha, R., Pressure–volume–temperature dependence of polypropylene/organoclay nanocomposites, *Macromolecules*, **37**, 10123–10133 (2004).
- Utracki, L. A., Simha, R., and Garcia-Rejon, A., Pressure–volume–temperature relations in nanocomposite, *Macromolecules*, **36**, 2114–2121 (2003).
- Vlasveld, D. P. N., Fibre reinforced polymer nanocomposites, Ph.D. dissertation, Technische Universiteit Delft, 2005.
- Vlasveld, D. P. N., Vaidya, S. G., Bersee, H. E. N., and Picken, S. J., A comparison of the temperature dependence of the modulus, yield stress and ductility of nanocomposites based on high and low MW PA6 and PA66, *Polymer*, **46**, 3452–3461 (2005a).
- Vlasveld, D. P. N., Bersee, H. E. N., and Picken, S. J., Creep and physical aging behaviour of PA6 nanocomposites, *Polymer*, **46**, 12539–12545 (2005b).

- Vlasveld, D. P. N., Groenewold, J., Bersee, H. E. N., and Picken, S. J., Moisture absorption in polyamide-6 silicate nanocomposites and its influence on the mechanical properties, *Polymer*, **46**, 12567–12576 (2005c).
- Wang, C. L., Hirade, T., and Maurer, F. H. J., Free-volume distribution and positronium formation in amorphous polymers: temperature and positron-irradiation-time dependence, *J. Chem. Phys.*, **108**, 4654–4661 (1998).
- Wool, R. P., Twinkling fractal theory of the glass transition, *J. Polym. Sci. B*, **46**, 2765–2778 (2008a).
- Wool, R. P., Self-healing materials: a review, *Soft Matter*, **4**, 400–418 (2008b).
- Wool, R. P., and Campanella, A., Twinkling fractal theory of the glass transition: rate dependence and time–temperature superposition, *J. Polym. Sci., Part B: Polym. Phys.*, **47**, 2578–2590 (2009).
- Xie, H., and Simha, R., Theory of solubility of gases in polymers, *Polym. Int.*, **44**, 348–355 (1997).
- Xie, H., Nies, E., and Stroeks, A., Some considerations on equation of state and phase relations: polymer solutions and blends, *Polym. Eng. Sci.*, **32**, 1654–1664 (1992).
- Zoller, P., Specific volume of polysulfone as a function of temperature and pressure, *J. Polym. Sci. Polym. Phys. Ed.*, **16**, 1261–1275 (1978).
- Zoller, P., in *Polymer Handbook*, 3rd ed., Brandrup, J., and Immergut, E. H., Eds., Wiley, New York, 1989.
- Zoller, P., and Hoehn, H. H., Pressure–volume–temperature properties of blends of poly(2,6-dimethyl-1,4-phenylene ether) with polystyrene, *J. Polym. Sci. Polym. Phys. Ed.*, **20**, 1385–1397 (1982).
- Zoller, P., and Walsh, D., *Standard Pressure–Volume–Temperature Data for Polymers*, Technomic, Lancaster, PA, 1995.